The transient response of floating elastic plates to wavemaker forcing in two dimensions

F. Montiel*, L.G. Bennetts[1], V.A. Squire

Department of Mathematics and Statistics, University of Otago, PO Box 56, Dunedin 9054, New Zealand

Abstract

The time-dependent linear motion in a two-dimensional fluid domain containing a group of floating thin elastic plates is considered. Forcing is provided by a wavemaker and the waves that transmit through the group of plates are partially reflected by a beach. Fourier Transforms are used to relate the solutions in the time and frequency-domain, where a solution is found using a combination of eigenfunction matching and transfer matrices. This allows reflections from the wavemaker and the beach to be included or excluded in a simple manner. Numerical results show that the frequency response of a single plate is significantly affected by the resonances introduced by the presence of the lateral boundaries. For a two-plate system the relative flexural response is found to be strongly dependent on plate spacing.

Key words: Linear water waves, Elastic plates, Time-domain, Wavemaker

1. Introduction

Interactions between surface gravity waves and floating compliant bodies have been studied extensively, particularly in the last two decades. Linear theory is often used along with thin elastic plate theory, and this has enabled a wide range of mathematical techniques to be developed. On the other hand, few wave tank experiments have taken place to validate these models. In support of research on Very Large Floating Structures (VLFSs), some experiments were conducted in the late 1990's in Japan (see, e.g., Yago and Endo, 1996; Ohta et al., 1997; Kagemoto et al., 1998), looking at the hydroelastic response of rectangular elastic plates for normal and oblique wave incidence. The aim of the experiments was to monitor the wave loads on a particular structure, scaled from the original full-size VLFS. More general studies are needed to understand how elastic structures of various thicknesses and shapes respond to waves across a wide frequency range. In this context, the most relevant series of experiments was conducted by S. Sakai and K. Hanai in Japan in a two-dimensional wave flume. These experiments were focused on determining the dispersion relation that characterises the propagation of flexural gravity waves in ice-covered seas (see Sakai and Hanai, 2002).

[1]Present address: School of Mathematical Sciences, University of Adelaide, Adelaide, South Australia, 5005, Australia
*Corresponding author. Tel.: +64 3 477 9099
Email address: fmontiel@maths.otago.ac.nz (F. Montiel)

The current authors, in collaboration with members of the *Laboratoire de Mécanique des Fluides* of *École Centrale de Nantes* (see, e.g., Roux de Reilhac et al., 2011), are involved in a series of wave tank experiments to extract the flexural response of a small group of circular compliant plates under linear wave conditions. It is expected that these experiments will produce benchmark results to validate a fully three-dimensional linear hydroelastic model. A description of the experimental campaign and preliminary results may be found in Montiel et al. (2011). While these experiments motivate the present work, modelling the hydroelastic interactions between a three-dimensional wave tank and an elastic scatterer presents a significant challenge. Although methods exist to calculate the circular wave field produced by a floe or floes (see Meylan, 2002; Peter and Meylan, 2004; Bennetts and Williams, 2010), it is not obvious how to couple this to the reflected wave field induced by the rectangular boundaries of the domain. The problem is much easier to solve in a two-dimensional setting, and this approximation delineates the scope of this study where the aim is to provide analytical insights concerning the flexural response of floating elastic plates due to a transient regular wave forcing produced by a wavemaker.

In the present paper, we propose a two-dimensional wave tank model, which includes a wavemaker and a beach, to characterise the transient hydroelastic response of a group of floating thin elastic plates. Although we introduce lateral boundaries to the fluid domain, no direct implications to the wave tank experiments mentioned previously is intended. The effects of the side walls and the wave propagation over the directional spectrum are not considered in the present two-dimensional model, and will be included in a future three-dimensional study.

Water wave scattering by floating elastic plates has been of interest in two main areas. The first application concerns the propagation of ocean waves into large fields of sea-ice floes in the polar seas. Research in this area has been summarised by Squire et al. (1995) and, more recently, by Squire (2007). The second area of application relates to the design of pontoon-type VLFSs mentioned above, such as offshore floating runways. Literature surveys on the hydroelastic response of VLFSs are due to Kashiwagi (2000a) and Watanabe et al. (2004).

Our model is based on potential flow theory. The equations are linearised, assuming that water surface oscillations are of small amplitude compared to the wavelength. The floating elastic plates are modelled as Euler-Bernoulli thin elastic beams, assuming the vertical deformations in a plate are small compared to its thickness. The vertical displacement of a plate then completely characterises its motion.

Unlike most hydroelastic models, the fluid domain is bounded laterally. At one end, a wavemaker exists; its motion transmitted to the fluid through a kinematic condition. At the opposite end, an absorbing beach reflects a fraction of the amplitude of the waves that reach it.

Finding a solution of the proposed model is challenging, as the equations are solved in the time-domain. A number of time-domain methods are available in the literature. The memory-effect and related Laplace transform methods have been widely used to solve the radiation problem (fluid initially at rest) of a thin

elastic plate in two dimensions (see, e.g., Kashiwagi, 2000b; Korobkin, 2000; Sturova, 2006; Meylan and Sturova, 2009). Those methods require a time stepping evaluation of the solution. The spectral generalised eigenfunction method, developed for a floating elastic plate by Hazard and Meylan (2007), allows for the transient response to be obtained for arbitrary initial conditions. The spectral method provides a mapping from the time-domain to the frequency-domain through a self-adjoint operator, so that the temporal evolution of the system may be obtained by calculating an integral over the corresponding harmonic excitations. This is similar to the approach adopted in the present work. However, because the system is initially at rest we may use a simple Fourier Transform as a map between the time and frequency domains. The transient response is then obtained after solving the governing equations for a sufficient number of frequencies through the inverse Fourier integral.

In the frequency domain, the problem resembles a number of existing models of linear wave scattering by ice floes. In particular, the scattering occurring at the transition between an open water region and an ice-covered sea (ice edge) was originally solved by Fox and Squire (1994) using an eigenfunction matching method (EMM). An EMM involves the decomposition of the fluid motion in each homogeneous region of the overall domain into an infinite sum of propagating and decaying waves. Truncated representations are then matched at their common interface and combined with fluid continuities in some manner to generate equations that determine the amplitudes (at least approximately). In Fox and Squire (1994) a minimisation of a residual error was applied to derive the final equations but different approaches have been developed subsequently. Usually inner-products of the continuity relations are taken with vertical modal functions over the fluid depth (see, e.g., Kohout et al., 2007). A three-dimensional application of this method was proposed by Peter et al. (2003) to solve for the single circular floe. Other solution methods are possible and may give superior convergence and may also allow for semi-infinite fluid depth. For example, Chung and Fox (2002) and Linton and Chung (2003) solved the semi-infinite ice sheet problem, using a Wiener-Hopf technique and residual calculus, respectively. However, EMMs remain popular due to their speed for reasonable accuracy and their versatility. In particular, they are the basis for the current models of wave attenuation through a vast array of ice floes in 2-D (Kohout and Meylan, 2008) and 3-D (Bennetts et al., 2010).

The current model extends these previous approaches by including lateral boundaries and a non-zero draught of the plates. The solution method is based on eigenfunction matching to calculate the scattering produced by a single plate's edge. It accounts for the singularity induced by the draught of the plate by use of appropriately weighted Gegenbauer polynomials (see Williams and Porter, 2009). From this canonical problem a transfer matrix is obtained that maps amplitudes of the waves on one side of a plate's edge to the other, which allows us to develop an iterative technique to extend the method to multiple plates. This approach is similar to the one used by Bennetts et al. (2009) to generate the solution to the scattering by periodic variations embedded in a continuous ice sheet.

The governing equations of the problem are given in §2, including the conditions at the wavemaker and

the beach. The transformation to the frequency-domain is defined in §3. The frequency-domain solution method, briefly outlined above, is developed in §4 and numerical results are presented in §5. The transient response of the system is analysed in terms of the strain energy in the plate. The influence of the lateral boundaries and multiple plates on this quantity is investigated. In particular, the steady-state response, as well as the maximum strain energy are analysed over a frequency range that is relevant to the dimensions of a prototype wave tank.

2. Mathematical model

We investigate the scattering of small-amplitude waves by a group of floating elastic plates in a two-dimensional fluid domain which is bounded laterally. Let x and z be the horizontal and vertical coordinates, and assume that the z-axis points upwards. A wavemaker, located at the left-hand boundary of the domain ($x = 0$), generates waves that will set the system in motion. At the right-hand end ($x = x_b$) a beach exists that partly attenuates the waves that reach it. We consider that the set of plates is included in a sub-domain bounded at its left-hand end at $x = x_l$, and at its right-hand end at $x = x_r$. The equilibrium fluid surface coincides with $z = 0$ and the depth of the fluid domain is assumed to be constant, H say. We denote $\Omega_l = \{x, z : 0 \leq x < x_l, -H \leq z \leq 0\}$ and $\Omega_r = \{x, z : x_r < x \leq x_b, -H \leq z \leq 0\}$ the two exterior open water regions, and Λ_l and Λ_r their respective free surfaces. It is reasonable to begin the analysis with a single plate before extending to multiple plates. We suppose that this single plate has a constant thickness h, which is small compared to its length L. Let $d = h\,(\rho/\rho_0)$ be the Archimedean draught of the plate, where ρ is the density of the plate and ρ_0 is the density of the fluid. We denote $\Omega = \{x, z : x_l \leq x \leq x_r, -H \leq z \leq -d\}$ the water domain upon which the plate is floating, and Λ the plate's underside surface. In addition, we define the vertical interfaces between the fluid regions as $\Upsilon_l = \{x, z : x = x_l, -H \leq z \leq -d\}$ and $\Upsilon_r = \{x, z : x = x_r, -H \leq z \leq -d\}$.

The plate is allowed to have heave and pitch motions but surge motion is not considered. The plate also experiences bending under wave forcing. Fig. 1 shows a schematic of the problem modelled.

2.1. Boundary value problem in the time-domain

We assume the Reynolds number is large enough that viscous effects in the fluid can be neglected. It follows that the flow is irrotational, so the velocity field can be written as the gradient of a scalar field, known as the velocity potential and denoted $\Phi(x, z, t)$. We also suppose the fluid is incompressible, so that Φ satisfies Laplace's equation

$$\nabla^2\Phi = 0, \quad \text{in} \quad \Omega_l \cup \Omega \cup \Omega_r, \tag{1}$$

where $\nabla = (\partial_x, \partial_z)$. Moreover, the floor of the fluid domain is impermeable, so that the no-flow condition

$$\partial_z\Phi = 0, \quad \text{at} \quad z = -H, \tag{2}$$

applies, and we express the linearised free-surface condition

$$\partial_t^2\Phi + g\partial_z\Phi = 0, \quad \text{on} \quad \Lambda_l \cup \Lambda_r, \tag{3}$$

where $g \approx 9.81\ \mathrm{m\,s^{-2}}$ is the acceleration due to gravity.

The flexural behaviour of the plate is modelled by Euler-Bernoulli beam theory. In doing so, we assume that the thickness of the plate and its deformation are sufficiently small compared to the plate's length. It then follows that the vertical displacement of the plate's middle plane, $\eta(x,t)$, fully describes its behaviour. With reference to Timoshenko and Woinowsky-Krieger (1959),

$$D\partial_x^4\eta + \rho h\partial_t^2\eta = P - P_0 - \rho_w g d, \quad \text{on} \quad \Lambda, \tag{4}$$

where D and ρ are respectively the flexural rigidity and density of the plate. The quantities $P = P(x,t)$ and P_0 are, respectively, the pressure on Λ and the atmospheric pressure, while $\rho_w g d$ is the buoyancy term. The pressure term in Eq. (4) is derived from the linearised version of Bernoulli's equation applied on Λ, assuming no cavitation between the plate and water surface. After substitution, we obtain

$$\left(D\partial_x^4 + \rho h\partial_t^2 + \rho_w g\right)\partial_z\Phi + \rho_w\partial_t^2\Phi = 0, \quad \text{on} \quad \Lambda, \tag{5}$$

where we have used the linearised kinematic surface condition $\partial_t\eta = \partial_z\Phi$ on Λ.

Because free bending in the plate is assumed, the bending moment and shearing stress must vanish at its ends. In terms of velocity potential this is expressed as

$$\partial_x^2\partial_z\Phi = \partial_x^3\partial_z\Phi = 0 \quad \text{at} \quad z = -d, \quad x = x_l,\, x_r. \tag{6}$$

The motion of the wavemaker, located at $x = 0$ (see Fig. 1), is described by the function $X(z,t)$, which represents the amplitude of the paddle linearised about $x = 0$. Fig. 2 shows the geometry of the hinged-flap wavemaker that we use in our model, although other shapes could be considered. Following Schäffer (1996), the motion of the paddle is expressed as $X(z,t) = f(z)X_0(t)$, where $f(z)$ is the shape function representing the paddle geometry and $X_0(t)$ is the time-dependent evolution of the wavemaker's amplitude at $z = 0$. In the present paper, we have

$$f(z) = \begin{cases} 1 + z/(H-l), & -(H-l) \le z \le 0, \\ \\ 0 & -H \le z < -(H-l). \end{cases} \tag{7}$$

The energy is transmitted to the fluid through the linearised kinematic condition

$$\partial_t X = \partial_x\Phi, \quad \text{at} \quad x = 0. \tag{8}$$

Most wave tank experiments are designed to generate accurately controlled waves by a wavemaker over a period of time long enough to reach a steady-state. For this reason, wave tanks are all equipped with an

absorbing zone, known as a beach, located at the opposite end from the wavemaker so that returning waves travelling back through the wave tank cause minimal interference with the generated wave field. Ideally a beach would absorb all of the wave energy incident on it, but in practice even the most efficient beaches reflect part of the energy. To account for this reflection in our model, the beach is simulated by a piston-like wave absorber that can extract part of the incoming wave energy depending on the frequency. This approach was introduced by Clément (1996), who included such a condition as part of a non-linear numerical wave tank BEM solver. Let $X_b(t)$ be the horizontal displacement of the wave absorber. A kinematic condition is prescribed, which is

$$\partial_t X_b = \partial_x \Phi \quad \text{at} \quad x = x_b. \tag{9}$$

In addition, the system is initially at rest. Therefore the initial conditions $\Phi(x, z, 0) = \eta(x, 0) = X(z, 0) = X_b(0) = 0$ are applied. This completes the set of governing equations.

2.2. Non-dimensionalisation

From here on we scale the spatial variables by the depth H and the time variables by $\sqrt{H/g}$. Therefore we can express the non-dimensional variables (denoted by an over bar) as

$$\bar{x} = \frac{x}{H}, \quad \bar{z} = \frac{z}{H}, \quad \bar{t} = \frac{t}{\sqrt{H/g}}, \quad \bar{X} = \frac{X}{H}, \quad \bar{X}_b = \frac{X_b}{H}, \quad \text{and} \quad \bar{\Phi} = \frac{\Phi}{H\sqrt{Hg}}.$$

For clarity, the overbars are dropped for the remainder of the text, with the understanding that the variables are non-dimensional. Note that Eqs. (1), (2), (6), (8) and (9) remain unchanged, while Eqs. (3) and (5) become

$$\partial_t^2 \Phi + \partial_z \Phi = 0, \quad \text{on} \quad \Lambda_l \cup \Lambda_r, \tag{10}$$

and

$$\left(\beta \partial_x^4 + \gamma \partial_t^2 + 1\right) \partial_z \Phi + \partial_t^2 \Phi = 0, \quad \text{on} \quad \Lambda, \tag{11}$$

where $\beta = D/\rho_w g H^4$ and $\gamma = d/H$.

3. Transformation to the frequency-domain

Whilst a direct solution of the time-dependent governing equations, as set out in the previous section, presents a challenge, the corresponding time-harmonic problem may be tackled using standard methods. Accordingly, a Fourier transformation of the time variables is used to recast the problem in the frequency-domain. For the present problem, we assume that the wavemaker forcing, characterised by $X_0(t)$, is a continuous real function of the time parameter and is causal, that is $X_0(t) = 0$ for $t < 0$. A typical profile

is $X_0(t) = R(t)\cos\omega_0 t$, where ω_0 is the radian frequency and $R(t)$ is the envelope function, which is defined by the finite time signal

$$R(t) = A_w\left(\frac{t\mathrm{H}\,(t) - (t-t_1)\,\mathrm{H}\,(t-t_1)}{t_1} + \frac{(t-T)\,\mathrm{H}\,(t-T) - (t-t_2)\,\mathrm{H}\,(t-t_2)}{T-t_2}\right),$$

where the function $\mathrm{H}\,(t)$ is the Heaviside step function and the parameters ω_0, t_1, t_2, T and A_w are non-dimensional. The initial linear ramp settles after t_1 at A_w and the decaying linear ramp starts at t_2 until rest at T. The wavemaker amplitude time-evolution profile is plotted in Fig. 3(a) for $A_w = 1$, $t_1 = 5$, $t_2 = 30$, $T = 40$ and $\omega_0 = \pi$. The decaying ramp has the effect of smoothing the system's return to its equilibrium position.

The time-dependent evolution of the function $X(z,t)$ determines the transient response of the system, once the geometry is set. As we intend to convert the equations to the frequency-domain (equivalent to the harmonic excitation problem), we must Fourier transform the wavemaker signal. Let $\widehat{X}$ define the one-sided Fourier transform of X, so that

$$\widehat{X}(z,\alpha) = \mathscr{F}[X(z,t)] = \int_0^\infty X(z,t)\,\mathrm{e}^{-\,\mathrm{i}\sqrt{\alpha}t}\,\mathrm{d}t = f(z)\mathscr{F}[X_0(t)], \tag{12}$$

where $\alpha = H\omega^2/g$ is a non-dimensional frequency parameter. For the present wavemaker forcing, the Fourier transform can be calculated analytically, the signal being non-zero during a finite duration. It can be shown that

$$\mathscr{F}[X_0(t)] = \frac{A_w}{2}\left[F\left(\sqrt{\alpha}-\sqrt{\alpha_0}\right) + F\left(\sqrt{\alpha}+\sqrt{\alpha_0}\right)\right],$$

where $\alpha_0 = H\omega_0^2/g$ and

$$F(\theta) = \frac{\mathrm{e}^{-\,\mathrm{i}\theta t_1} - 1 + \,\mathrm{i}\theta t_1\,\mathrm{e}^{-\,\mathrm{i}\theta T}}{t_1\theta^2} + \frac{\mathrm{e}^{-\,\mathrm{i}\theta t_2} - (1 + \,\mathrm{i}\theta\,(T-t_2))\,\mathrm{e}^{-\,\mathrm{i}\theta T}}{(T-t_2)\,\theta^2}, \quad \theta \in \mathbb{R}^*.$$

For the set of parameters defined above, the real and imaginary parts of $\mathscr{F}[X_0(t)]$, which are related through the Kramers-Kronig relations, are given in Fig. 3(b). We recover the original time-dependent signal by an inverse Fourier transformation

$$X(z,t) = \mathscr{F}^{-1}[\widehat{X}] = \frac{1}{2\pi}\int_{-\infty}^{\infty}\widehat{X}(z,\alpha)\,\mathrm{e}^{\,\mathrm{i}\sqrt{\alpha}t}\,\mathrm{d}\sqrt{\alpha}.$$

Likewise, the pair of transforms for the velocity potential is written

$$\widehat{\Phi}(x,z,\alpha) = \int_0^\infty \Phi(x,z,t)\,\mathrm{e}^{-\,\mathrm{i}\sqrt{\alpha}t}\,\mathrm{d}t \quad \text{and} \quad \Phi(x,z,t) = \frac{1}{2\pi}\int_{-\infty}^{\infty}\widehat{\Phi}(x,z,\alpha)\,\mathrm{e}^{\,\mathrm{i}\sqrt{\alpha}t}\,\mathrm{d}\sqrt{\alpha},$$

and, for the wave absorber's displacement, it is

$$\widehat{X}_b(\alpha) = \int_0^\infty X_b(t)\,\mathrm{e}^{-\,\mathrm{i}\sqrt{\alpha}t}\,\mathrm{d}t \quad \text{and} \quad X_b(t) = \frac{1}{2\pi}\int_{-\infty}^{\infty}\widehat{X}_b(\alpha)\,\mathrm{e}^{\,\mathrm{i}\sqrt{\alpha}t}\,\mathrm{d}\sqrt{\alpha}.$$

Taking the Fourier transform of Eqs. (1), (2), (6), (8), (9), (10) and (11), we obtain the following set of PDEs that describes the problem in the frequency-domain

$$\nabla^2\widehat{\Phi} = 0, \qquad (x,z) \in \Omega_l \cup \Omega \cup \Omega_r, \tag{13a}$$

$$\partial_z\widehat{\Phi} = 0, \qquad z = -H, \tag{13b}$$

$$\partial_z\widehat{\Phi} = \alpha\widehat{\Phi}, \qquad (x,z) \in \Lambda_l \cup \Lambda_r, \tag{13c}$$

$$\left(\beta\partial_x^4 - \alpha\gamma + 1\right)\partial_z\widehat{\Phi} = \alpha\widehat{\Phi}, \quad (x,z) \in \Lambda, \tag{13d}$$

$$\partial_x^2\partial_z\widehat{\Phi} = \partial_x^3\partial_z\widehat{\Phi} = 0, \qquad z = -d, \quad x = x_l \quad \text{and} \quad x = x_r, \tag{13e}$$

$$i\sqrt{\alpha}\widehat{X} = \partial_x\widehat{\Phi}, \qquad x = 0, \tag{13f}$$

$$i\sqrt{\alpha}\widehat{X}_b = \partial_x\widehat{\Phi}, \qquad x = x_b. \tag{13g}$$

The frequency-domain boundary value problem is then completely determined by the frequency parameter α, and the properties of the plate β and γ. To obtain the transient response of the system, this set of frequency-dependent equations must be solved over a range of frequencies that is determined by the spectral distribution of the input variable, $X_0(t)$ (see Fig. 3(b)). A solution method for these equations will be outlined in the subsequent section.

In practice, we take advantage of the particular spectral distribution, which is narrowband around the exciting frequency ω_0. Once the system of PDEs is solved for a sufficient number of frequencies, the time-domain solution is reconstructed by evaluating the inverse Fourier integral of the potential $\widehat{\Phi}$. Several integration schemes have been compared for this purpose: the Fast Fourier Transform (FFT) algorithm, a direct integration rule and a numerical quadrature method based on a double exponential formula (see Ooura, 2005). We performed tests on the wavemaker input signal $X_0(t)$ and it was found that the FFT was superior in both accuracy and speed. Such performances are explained as the FFT only requires $\mathrm{O}(N_s \log N_s)$ operations to compute the transform, where N_s is the number of frequency samples, while direct integration requires an inversion at each time sample so that $\mathrm{O}(N_s N_t)$ operations are needed, where N_t is the number of time samples. In implementing the FFT inversion, an ideal low-pass filter (sinc filter) is applied to the frequency-domain variables by truncating the spectrum at an appropriate maximum frequency to limit the number of frequency samples. This induces distortion in the reconstructed time signal in the form of small ripples, and is characteristic of the truncation of Fourier series (here the Discrete Fourier expansion used by the FFT), commonly called the Gibbs phenomenon. Although we can observe these oscillations on the time responses, they are small enough not to affect the results.

4. Frequency-domain solution method

4.1. Expansion of the velocity potential

We partition the fluid domain into 3 subdomains, as shown in Fig. 4. In each region, the potential is expressed as the sum of two components $\widehat{\Phi}_i^{(\pm)}$ $(i = l, r)$, for the exterior regions, and $\widehat{\Phi}^{(\pm)}$, for the interior region, where the superscript denotes the direction in which the wave propagates or decays. In open water regions (Ω_l and Ω_r), we approximate the potential as follows

$$\widehat{\Phi}_i^{(\pm)}(x,z) \approx \sum_{n=0}^{N} \left[A_i^{(\pm)}\right]_n e^{\mp k_n (x - x_i^{(\pm)})} \varphi_n(z) \quad (i = l, r), \tag{14}$$

where the vertical modes are $\varphi_n(z) = \cos k_n(z+H)/\cos k_n H$ and we have truncated the infinite sums to N terms. The quantities k_n are the roots K of the free-surface dispersion relation

$$K \tan KH = -\alpha,$$

with k_0 on the positive imaginary axis, and k_n $(n = 1, \ldots, N)$ real, positive and in ascending order. The exponential functions, used to describe the horizontal motions, are associated with incident, reflected and transmitted travelling waves $(n = 0)$ and also decaying waves that are only excited in the vicinity of the plate's edges $(n = 1, \ldots, N)$. In Eq. (14), the abscissa $x_i^{(\pm)}$ $(i = l, r)$ corresponds to the location where the particular wave is generated, so that $x_l^{(+)} = 0$, $x_l^{(-)} = x_l$, $x_r^{(+)} = x_r$ and $x_r^{(-)} = x_b$. We can rewrite expansion (14) using matrix and vector notations as

$$\widehat{\Phi}_i^{(\pm)}(x,z) \approx \mathbf{C_0}(z)\mathbf{E}_0^{(\pm)}(x - x_i^{(\pm)})\mathbf{A}_i^{(\pm)} \quad (i = l, r), \tag{15}$$

where $\mathbf{A}_i^{(\pm)}$ is the $(N+1)$-length column vector of the unknown amplitudes defined in Eq. (14). The row vector $\mathbf{C_0}(z) = (\varphi_0(z), ..., \varphi_N(z))$ and the diagonal matrix $\mathbf{E}_0^{(\pm)}(x) = \operatorname{diag}\left\{e^{\mp k_0 x}, \ldots, e^{\mp k_N x}\right\}$ have also been introduced.

In region Ω, we approximate the potential as

$$\widehat{\Phi}^{(\pm)}(x,z) \approx \sum_{n=-2}^{N} \left[A^{(\pm)}\right]_n e^{\mp \kappa_n (x - x^{(\pm)})} \psi_n(z), \tag{16}$$

where the vertical modes are $\psi_n(z) = \cos \kappa_n(z+H)/\cos \kappa_n(H-d)$, defined for all $n \geq -2$, and the truncation parameter N is used again. The quantities κ_n are the roots K of the plate-covered dispersion relation

$$\left(\beta K^4 + 1 - \alpha\gamma\right) K \tan K(H-d) = -\alpha,$$

where we denote the unique root that lies on the positive imaginary axis as κ_0, and the positive real roots $\kappa_n\,(n \geq 1)$, which are ordered in ascending magnitude. In this case there also exists a pair of complex conjugate roots with positive real part, denoted κ_{-2} and κ_{-1}, that support damped modes (travelling waves

that decay with distance from the scattering source). Bennetts et al. (2007) proved that the vertical modes $\psi_n(z)$ $(n \geq -2)$ are not linearly independent and the degree by which this set of vertical modes can be reduced is two. It follows that

$$\psi_{-j}(z) = \sum_{n=0}^{\infty} v_{n,j}\psi_n(z), \quad j = 1, 2. \tag{17}$$

The coefficients $v_{n,j}$ are expressed, following Bennetts (2007), as

$$v_{n,j} = \frac{\kappa_n \mathcal{R}'(\kappa_{-j})(\kappa_n^2 - \kappa_{-j^*}^2)\cos\kappa_n(H-d)}{\kappa_{-j}\mathcal{R}'(\kappa_n)(\kappa_{-j}^2 - \kappa_{-j^*}^2)\cos\kappa_{-j}(H-d)}, \quad n \geq 0,$$

where $j^* = (3-(-1)^j)/2$ and the prime superscript signals the derivative of the single variable function it is applied to. We have also defined the following complex function

$$\mathcal{R}(\xi) = (1 - \alpha\gamma + \beta\xi^4)\xi\sin\xi(H-d) + \alpha\cos\xi(H-d), \quad \xi \in \mathbb{C}.$$

Applying the free edge conditions (13e) to $\widehat{\Phi}^{(\pm)}$ allows us to express the amplitudes of the damped modes in terms of the amplitudes $(A^{(\pm)})_n$ $(n = 0, \ldots, N)$, so that

$$\left[\mathbf{A}^{(\pm)}\right]_{-j} = \mathbf{T}_{1j}^{(\pm)}\mathbf{A}^{(+)} + \mathbf{T}_{2j}^{(\pm)}\mathbf{A}^{(-)}, \quad j = 1, 2, \tag{18}$$

where

$$\mathbf{A}^{(\pm)} = \left(\left[A^{(\pm)}\right]_0, \ldots, \left[A^{(\pm)}\right]_N\right)^{\mathrm{T}}.$$

Expressions for the row vectors $\mathbf{T}_{ij}^{(\pm)}$ $(i, j = 1, 2)$ can be found in A, and use Eq. (17), with the infinite sum truncated to N. We therefore write

$$\widehat{\Phi}^{(\pm)}(x, z) = \mathbf{C}(z)\mathbf{D}^{(\pm)}(x)\mathbf{A}^{(+)} + \mathbf{C}(z)\mathbf{E}^{(\mp)}(x)\mathbf{A}^{(-)}, \tag{19}$$

where $\mathbf{C}(z) = (\psi_0(z), ..., \psi_N(z))$. The $(N+1)$-size square matrices $\mathbf{D}^{(\pm)}(x)$ and $\mathbf{E}^{(\mp)}(x)$ are obtained by substituting Eqs. (18) into Eq. (16). The coefficients of the matrices $\mathbf{D}^{(\pm)}(x)$ and $\mathbf{E}^{(\mp)}(x)$ are, as follows

$$\left[D^{(\pm)}\right]_{n,p} = \delta_{n,p}\,\mathrm{e}^{\mp\kappa_n(x-x^{(\pm)})} + \sum_{j=1}^{2}\left[T_{1j}^{(\pm)}\right]_p v_{n,j}\,\mathrm{e}^{\mp\kappa_{-j}(x-x^{(\pm)})},$$

$$\left[E^{(\pm)}\right]_{n,p} = \delta_{n,p}\,\mathrm{e}^{\mp\kappa_n(x-x^{(\pm)})} + \sum_{j=1}^{2}\left[T_{2j}^{(\pm)}\right]_p v_{n,j}\,\mathrm{e}^{\mp\kappa_{-j}(x-x^{(\pm)})},$$

where $\delta_{n,p} = 1$ if $n = p$ and 0 otherwise. We also introduce the two matrices $\mathbf{D}(x) = \mathbf{D}^{(+)}(x) + \mathbf{D}^{(-)}(x)$ and $\mathbf{E}(x) = \mathbf{E}^{(+)}(x) + \mathbf{E}^{(-)}(x)$, for convenience.

4.2. Scattering by a plate's edge

A version of eigenfunction matching method (EMM) is used to calculate the scattering at a plate's edges. The method is demonstrated for the left-hand edge, which is located at $x = x_l$. On the fluid column at this location we enforce continuity of fluid pressure and velocity. To do this the function $u_l(z)$ is introduced, which is defined as the fluid normal velocity along Υ_l. The continuities are then expressed as

$$\widehat{\Phi}_l(x_l, z) = \widehat{\Phi}(x_l, z) \quad \text{and} \quad \partial_x \widehat{\Phi}_l(x_l, z) = \partial_x \widehat{\Phi}(x_l, z) = u_l(z),$$

for $z \in \Upsilon_l$, where $\widehat{\Phi}_l = \widehat{\Phi}_l^{(+)} + \widehat{\Phi}_l^{(-)}$ and $\widehat{\Phi} = \widehat{\Phi}^{(+)} + \widehat{\Phi}^{(-)}$. Additionally, the no surge assumption is applied as $\partial_x \widehat{\Phi}_1(x_l, z) = 0$, $-d \leq z \leq 0$.

The submerged corner creates a singularity in the fluid velocity. Numerical evidence suggests that this singularity is of the same order as that in the case of a rigid plate of the same shape, i.e. it is of order $-1/3$ (Williams and Porter, 2009). Following Bennetts and Williams (2010), we capture this singularity by approximating the function u_l as a sum of, appropriately weighted, even Gegenbauer polynomials. We define the set of polynomials as $\mathcal{V}_g = \left\{ \mathfrak{C}_{2m}^{(1/6)}(z^*) : m \in \mathbb{N} \right\}$, where we have introduced $z^* = (z + H) / (H - d) \in (0, 1)$. Therefore let

$$u_l(z) \approx \sum_{m=0}^{M} U_m^{(l)} \mathfrak{C}_{2m}^{(1/6)}(z^*), \tag{20}$$

where the infinite sum has been truncated to $M + 1$ modes, chosen such that convergence towards $u_l(z)$ is satisfactory. We express the elements of $\mathcal{V}_g$ as

$$\mathfrak{C}_m^{(\delta)}(y) = \frac{2}{(H-d)} \frac{m!(m+\delta)\Gamma^2(\delta)}{\pi 2^{1-2\delta}\Gamma(m+2\delta)} \left(1 - y^2\right)^{\delta - 1/2} G_m^{(\delta)}(y), \quad 0 \leq y \leq 1,$$

with Γ the Gamma function and $G_m^{(\delta)}(y)$ a Gegenbauer polynomial (see, Abramowitz and Stegun, 1970, §22). For convenience in what follows, we re-express the previous expansion as

$$u_l(z) = \mathbf{C_g}(z^*)\mathbf{U_l}, \tag{21}$$

where $\mathbf{U_l} = (U_0^{(l)}, ..., U_M^{(l)})^{\mathrm{T}}$ and $\mathbf{C_g}(z^*) = (\mathfrak{C}_0(z^*), ..., \mathfrak{C}_{2M}(z^*))$. The subscript g denotes a quantity associated with the Gegenbauer projection basis, and the subscript l denotes a quantity associated with the plate's left edge.

Using the matrix expansions of the potential defined in the previous section, we apply the EMM as

$$\begin{cases} \mathbf{B_0} \left(\mathbf{E}_0^{(+)'}(x_l)\mathbf{A}_l^{(+)} + \mathbf{E}_0^{(-)'}(0)\mathbf{A}_l^{(-)} \right) = \mathbf{B_{g0}}\mathbf{U_l}, \\ \\ \mathbf{B} \left(\mathbf{D}'(x_l)\mathbf{A}^{(+)} + \mathbf{E}'(x_l)\mathbf{A}^{(-)} \right) = \mathbf{B_g}\mathbf{U_l}, \end{cases} \tag{22}$$

to approximate the continuity of fluid velocity, and

$$\mathbf{B_{g0}}^{\mathrm{T}} \left(\mathbf{E}_0^{(+)}(x_l)\mathbf{A}_l^{(+)} + \mathbf{A}_1^{(-)} \right) = \mathbf{B_g}^{\mathrm{T}} \left(\mathbf{D}(x_l)\mathbf{A}^{(+)} + \mathbf{E}(x_l)\mathbf{A}^{(-)} \right), \tag{23}$$

for the continuity of fluid pressure, noting that $\mathbf{E_0^{(-)}}(0)$ is the identity matrix of dimension $N+1$.

In the above, the $(N+1)$-size square matrices $\mathbf{B_0}$ and $\mathbf{B}$ respectively contain the inner-products of the vertical modes of $\mathcal{V}_0 = \{\varphi_n(z) : n \in \mathbb{N}\}$ and the elements of $\mathcal{V} = \{\psi_n(z) : n \in \mathbb{N}\}$, and are defined as

$$[\mathbf{B_0}]_{i+1,j+1} = \int_{-H}^{0} \varphi_i \varphi_j \,\mathrm{d}z \quad \text{and} \quad [\mathbf{B}]_{i+1,j+1} = \int_{-H}^{-d} \psi_i \psi_j \,\mathrm{d}z \quad (i,j = 0,\ldots,N)\,.$$

Similarly, we introduced $\mathbf{B_{g0}}$, the matrix of inner-products between the elements of $\mathcal{V}_0$ and $\mathcal{V}_g$, and $\mathbf{B_g}$, the matrix of inner-products between the elements $\mathcal{V}$ and $\mathcal{V}_g$. These matrices are non-square and have dimension $(N+1)\times(M+1)$. The entries are calculated using Gegenbauer's addition theorem (see, Williams and Porter, 2009) and the orthogonality of the Gegenbauer polynomials. They are given by

$$[\mathbf{B_{g0}}]_{i+1,j+1} = \int_{-H}^{-d} \varphi_i \mathfrak{C}_j(z^*(z)) \,\mathrm{d}z = \Gamma(\delta) \left(\frac{2}{k_i(H-d)}\right)^{\delta} (2j+\delta)\,(-1)^j \,\frac{\mathrm{J}_{2j+\delta}\left(k_i(H-d)\right)}{\cos k_i H},$$

and

$$[\mathbf{B_g}]_{i+1,j+1} = \int_{-H}^{-d} \psi_i \mathfrak{C}_j(z^*(z)) \,\mathrm{d}z = \Gamma(\delta) \left(\frac{2}{\kappa_i(H-d)}\right)^{\delta} (2j+\delta)\,(-1)^j \,\frac{\mathrm{J}_{2j+\delta}\left(\kappa_i(H-d)\right)}{\cos \kappa_i\,(H-d)},$$

where J_p is the Bessel function of the first kind of order p.

Allowing N and M to be independent provides more numerical freedom, as their effect on the accuracy and convergence rate can be studied separately. Consequently, non-square matrices appear and care must be taken to manipulate them. The solution is found by expressing the vectors of amplitude of the scattered waves, i.e. $\mathbf{A}_l^{(-)}$ and $\mathbf{A}^{(+)}$, in terms of the vectors of amplitude of the incident waves and the interface vector $\mathbf{U_l}$. We eliminate this vector using Eq. (23), in which an $(M+1)$-size square matrix appears that can be inverted.

We may calculate the scattering matrix for the plate's edge. It is denoted $\mathbf{S_l}$, and maps the amplitudes of the waves incident on the left edge of the plate to the amplitudes of the scattered waves induced by it. Alternatively, we may express the amplitudes of the waves in the plate-covered fluid region in terms of the amplitudes in the open fluid region, through transfer matrix $\mathbf{T_l}$. The matrices $\mathbf{S_l}$ and $\mathbf{T_l}$ are defined by

$$\begin{pmatrix} \mathbf{A}_l^{(-)} \\ \mathbf{A}^{(+)} \end{pmatrix} = \mathbf{S_l} \begin{pmatrix} \mathbf{A}_l^{(+)} \\ \mathbf{A}^{(-)} \end{pmatrix} \quad \text{and} \quad \begin{pmatrix} \mathbf{A}^{(+)} \\ \mathbf{A}^{(-)} \end{pmatrix} = \mathbf{T_l} \begin{pmatrix} \mathbf{A}_l^{(+)} \\ \mathbf{A}_l^{(-)} \end{pmatrix}, \tag{24}$$

and their entries may be related in a straightforward manner (see Bennetts and Squire, 2009). Similar expressions can be obtained for the plate's right-hand edge, where we denote the respective scattering and transfer matrices by $\mathbf{S_r}$ and $\mathbf{T_r}$. This means that we may write the transfer matrix for the plate, $\mathbf{T}$ say, as the simple expression $\mathbf{T} = \mathbf{T_r}\mathbf{T_l}$.

The matrices $\mathbf{T_l}$ and $\mathbf{T_r}$ are closely related due to the symmetry of the plate, as one maps from the open water region to the plate-covered region and the other, vice-versa. However, they are not direct inverses of one another, as the phases of the incident and reflected waves are different at each edge. Note that $\mathbf{T}$ depends on the plate's length and thickness.

4.3. Scattering by multiple plates

We now consider the case in which there are two plates, separated by a free-surface region, and which may have different properties. We re-partition the fluid domain into 5 fluid regions; the two exterior open water regions Ω_p $(p = l, r)$, the two plate regions Ω_q $(q = 1, 3)$ and the interior open water region Ω_2. They are contained in the respective intervals $(x_i^{(+)}, x_i^{(-)})$, such that $x_l^{(+)} = 0$, $x_l^{(-)} = x_1^{(+)} = x_l$, $x_1^{(-)} = x_2^{(+)}$, $x_2^{(-)} = x_3^{(+)}$, $x_3^{(-)} = x_r^{(+)} = x_r$ and $x_r^{(-)} = x_b$. We denote the potentials in the 5 regions $\widehat{\Phi}_i(x, z)$ accordingly. In regions Ω_i, $i = l, 2, r$, they are given by Eq. (15), while in plate-covered fluid regions Ω_i, $i = 1, 3$, they are expressed as

$$\widehat{\Phi}_i(x, z) = \mathbf{C}_i(z) \left(\mathbf{D}_i(x) \mathbf{A}_i^{(+)} + \mathbf{E}_i(x) \mathbf{A}_i^{(-)} \right), \quad i = 1, 3. \tag{25}$$

The vector $\mathbf{C}_i(z)$ and the matrices $\mathbf{D}_i(x)$ and $\mathbf{E}_i(x)$ denote the corresponding arrays $\mathbf{C}(z)$, $\mathbf{D}(x)$ and $\mathbf{E}(x)$ when evaluated using the properties of the plate in region Ω_i.

Using the solution method described in §4.2, we define $\mathbf{T_1}$ and $\mathbf{T_3}$ as the transfer matrices associated with plates in regions Ω_1 and Ω_3, respectively. The use of transfer matrices provides an efficient means of combining the interactions of multiple plates. In particular, we can map the vectors of amplitudes in Ω_l to the ones in Ω_r as follows

$$\begin{pmatrix} \mathbf{A}_r^{(+)} \\ \mathbf{A}_r^{(-)} \end{pmatrix} = \mathbf{T} \begin{pmatrix} \mathbf{A}_l^{(+)} \\ \mathbf{A}_l^{(-)} \end{pmatrix}, \tag{26}$$

where $\mathbf{T} = \mathbf{T}_3 \mathbf{T}_1$ is the transfer matrix associated with the group of plates. This procedure can be generalised to an arbitrary number of plates in a straightforward manner. To do this, the transfer matrix, $\mathbf{T}$, associated with the corresponding group of plates is obtained by multiplying the transfer matrices associated with each individual plate. The scattering matrix $\mathbf{S}$ associated with the group of plates is then obtained from the entries of $\mathbf{T}$, so we have

$$\begin{pmatrix} \mathbf{A}_l^{(-)} \\ \mathbf{A}_r^{(+)} \end{pmatrix} = \mathbf{S} \begin{pmatrix} \mathbf{A}_l^{(+)} \\ \mathbf{A}_r^{(-)} \end{pmatrix}. \tag{27}$$

4.4. Wavemaker forcing and beach reflection

The solution method for the first-order wavemaker is well-known (see, e.g., Linton and McIver, 2001) and we only rewrite the method (EMM) here so the relation with our previous notations is apparent. The scattering condition is developed by integrating Eq. (13f) multiplied by $\mathbf{C_0}^{\mathrm{T}}(z)$ over the vertical domain, so we obtain the following matrix equation

$$i\sqrt{\alpha}\widehat{X}_0 \mathbf{F} = \mathbf{B_0} \left(\mathbf{E}_0^{(+)'}(0) \mathbf{A}_l^{(+)} + \mathbf{E}_0^{(-)'}(-x_l) \mathbf{A}_l^{(-)} \right), \tag{28}$$

where we have introduced the $(N + 1)$-length vector

$$\mathbf{F} = \int_{-H}^{0} f(z) \mathbf{C_0}^{\mathrm{T}}(z) \, \mathrm{d}z,$$

which has entries that may be calculated using standard techniques. We may re-arrange Eq. (28) to obtain the vector of amplitudes of the waves generated in terms of the incoming wave amplitudes $\mathbf{A}_l^{(-)}$, and the external forcing vector $\mathbf{F_0}$, as

$$\mathbf{A}_l^{(+)} = \mathbf{S_0}\mathbf{A}_l^{(-)} + \mathbf{F_0}. \tag{29}$$

The $(N+1)$-size square matrix $\mathbf{S_0}$ and $(N+1)$-length vector $\mathbf{F_0}$ are easily calculated by re-arranging (28).

On the far end of the fluid domain ($x = x_b$), we may expand the reflective beach condition. We consider a reflection coefficient of magnitude $\mathcal{R}_b$, between 0 and 1, which depends on the frequency $\sqrt{\alpha}$ as

$$\mathcal{R}_b(\alpha) = 0.9\left(\mathrm{e}^{-5\sqrt{\alpha}} - 1\right) + 1, \tag{30}$$

which qualitatively characterises the reflection spectrum of a typical beach in a wave tank (see, e.g., Bonnefoy et al., 2006b). We also assume the beach does not reflect evanescent waves, assuming the plates are far enough from this boundary. This approach is equivalent to ignoring the vertical dependence and expressing the condition at $z = 0$. As a consequence, the control law of the wave absorber's displacement $\widehat{X}_b$ is defined such that a single travelling mode is generated at $x = x_b$ as follows

$$\mathbf{C_b}\widehat{\Phi}_r^{(-)}(x_b, 0) = \mathcal{R}_b\mathbf{C_b}\widehat{\Phi}_r^{(+)}(x_b, 0), \tag{31}$$

where $\mathbf{C_b} = (1, 0, \ldots, 0)^{\mathrm{T}}$ is a $(N+1)$-length vector. Using Eq. (14) and re-arranging allows us to express the beach condition as a matrix equation

$$\mathbf{A}_r^{(-)} = \mathbf{S_b}\mathbf{A}_r^{(+)}, \tag{32}$$

where $\mathbf{S_b} = \mathcal{R}_b\mathbf{C_b}\mathbf{C_0}(0)\mathbf{E}_0^{(+)}(x_b - x_r)$ is the scattering matrix associated with the beach.

The solution of the problem can now be obtained, for any frequency $\sqrt{\alpha}$, by solving the coupled system of matrix equations of size $N+1$ defined by Eqs. (27), (29) and (32), for an arbitrary number of plates. The solution method is based on multiple substitutions and is straightforward to implement.

The solution method for the frequency-domain problem, which is described above, is highly efficient. In particular, we note that, in most cases, only 5 Gegenbauer polynomials are required to capture the fluid velocity beneath the plate's edge to four decimal place accuracy. It is therefore possible to solve for the $\mathrm{O}(10^2$–$10^3)$ frequencies required, depending on the sampling frequency and the signal duration, to produce the time-dependent response.

5. Numerical results

The numerical results presented in this section concentrate on the flexure of the plate (or plates) under wavemaker forcing. Our intention is that these results may give some insights into issues arising from typical

laboratory experiments in two-dimensional wave flumes, such as the influence of the transient response and the boundaries of the fluid domain. Although the experimental campaign mentioned in the Introduction is not intended to be directly related to the results and conclusions drawn in the present section, we have chosen values for the parameters in accordance with the experimental setup described in Montiel et al. (2011).

In the subsequent computations, we have set $H = 2\,\mathrm{m}$ and $x_b = 15\,\mathrm{m}$ as the dimensions of the fluid domain, and the wavemaker paddle is hinged such that $l = 0.3\,\mathrm{m}$. The elastic properties of the plates, made of expanded PVC, are described by $E = 500\,\mathrm{MPa}$ and $\rho = 500\,\mathrm{kg\,m^{-3}}$, which are values that are similar to typical sea-ice when scaled. Additionally, it is appropriate to set the plate's length to be constant, $L = 1.5\,\mathrm{m}$ say, so the plate length to wavelength ratio only varies with the frequency, and we set $x_l = 10\,\mathrm{m}$. The initial ramp of the wavemaker time evolution is chosen following typical experimental values to be $t_1 = 2\,\mathrm{s}$. We generate results for three plate thicknesses, namely $h = 3$, 5 and 10 mm, as they are common values for the material utilised here.

5.1. Strain energy

The strain energy of a plate is an integrated value of the bending over the length of the plate. Following Timoshenko and Woinowsky-Krieger (1959), the strain energy of a two-dimensional plate, located between $x = l$ and $x = r$, is given by

$$V = \frac{1}{2} D \int_l^r \left(\partial_x^2 \eta\right)^2 \,\mathrm{d}x, \tag{33}$$

where $\partial_x^2 \eta$ is the curvature. We scale the strain energy by the incident wave energy, i.e. $\rho_0 g I_0^2/2$, where I_0 is the steady-state amplitude of the wave generated.

5.2. Frequency response of a single plate

We begin by analysing the frequency spectrum of the strain energy for a single plate. It is noted that linear models are characterised by resonances, typically due to phase interactions. However, in a wave tank we expect that such effects would be tempered by auxiliary physical processes and therefore would not be replicated exactly, if at all.

To understand how the wavemaker and the beach influence the flexural response of the plate, we study four cases. In case 1, we set the beach reflection coefficient to be 0 (perfect beach) and we also assume that the wavemaker is invisible to waves travelling from right to left, so we have no reflection on both lateral boundaries. This case is equivalent to the frequency response of a single plate in an unbounded domain (studied by a number of previous authors, e.g., Meylan and Squire, 1994). In case 2, the wavemaker reflects waves but the beach is still perfect ($\mathcal{R}_b = 0$), while in case 3, the wavemaker is invisible and the beach induces reflection dependent on the frequency, as described by Eq. (30). In case 4, both wavemaker and beach reflect waves.

In Fig. 5, the scaled strain energy is plotted against frequency for the three thicknesses mentioned above. We choose a frequency range, $f = 0.5$–$1.5\,\mathrm{Hz}$, corresponding to wavelengths $\lambda \approx 0.7$–$6\,\mathrm{m}$. We compare the influence of the domain lateral boundaries on the response using cases 1 (dashed line) and 4 (solid line). While the flexural response varies smoothly when no lateral reflections are considered, the presence of the wavemaker and the beach clearly disturbs the spectra. Primarily the incident wave passes through the plate but lateral reflections add a structure over this. The resonances correspond to natural modes of the system {Tank+Plate}.

Fig. 6 displays results similar to those in Fig. 5(b) (i.e. for the 5 mm plate only) but for an extended frequency spectrum. Even though it is unrealistic to generate such waves in real wave tanks, the larger bandwidth is used to highlight the influence of the beach and the wavemaker. Their effects are analysed separately. In Fig. 6(a), we look at the influence of the wavemaker. The solid line represents the flexural response spectrum when the beach is not present (case 2). Case 1 is given for reference as a dashed line. We note that, for case 2, the magnitudes of the resonance peaks vary smoothly with frequency and a trend envelope drives the evolution of those peaks. This envelope coincides with the case 1 curve, when the latter reaches a maximum. Those maxima correspond to the plate's natural modes. Meylan and Squire (1994) noticed that the resonances in flexure for case 1 occur when the reflection coefficient of the plate is zero. As the waves generated by the wavemaker are perfectly transmitted and no beach is present, case 1 and case 2 are equivalent at those frequencies. Fig. 6(c) shows the reflection coefficient spectrum and confirms these remarks.

In Fig. 6(b), we analyse the effects of the beach on the flexural response of the plate (case 3 as a solid line and case 1 as a thick dashed line for reference). The beach acts like a wall which attenuates most of the incident wave's energy, so the magnitudes of the resonance peaks are significantly smaller than those induced by the wavemaker (wall with no attenuation). We notice that the succession of peaks also fits in a smoothly varying envelope. The main difference with case 2 is that the resonance envelope reaches its maxima at the same frequencies as in case 1. Perfect transmission (see Fig. 6(c)) allows all the wave energy to reach the beach, inducing waves of larger amplitude there, so the natural modes of the system {Plate+Beach} have higher peaks. Although difficult to see, it is also noted that the resonance envelope and the response of case 1 match at $f = 1.09\,\mathrm{Hz}$ and $f = 1.99\,\mathrm{Hz}$, corresponding to the cases in which the beach has no effect on the response.

As the draught of the plate is taken into account in the present model, we can analyse the effect it has on the results compared to the commonly used shallow-draught approximation. In Fig. 6(b) and (c), the strain energy and reflection coefficient spectra are given as dotted lines to allow comparisons to be made. For this plate's thickness, the frequency responses seem to stretch towards high frequencies compared to the ones when draught is included, suggesting that high frequencies are more affected than low frequencies. A similar influence was found for other thicknesses, although the results are not shown in the present paper.

5.3. Transient response of a single plate

In this section, we analyse the transient evolution of the scaled strain energy, V. We are particularly interested in the influence of the fluid domain's lateral boundaries on generating strain energy of high magnitude after the wavefront has passed, due to multiple reflections, as well as the corresponding response time, defined as the time it takes for the system to reach its steady-state. Fig. 7 shows the time-dependent evolution of a single plate's strain energy until it reaches steady-state. Fig. 7(a)–(c) displays the flexural response of 3, 5 and 10 mm-thick plates at $f = 0.87$ Hz, respectively. Similarly, Fig. 7(d)–(f) give the respective responses at $f = 1.4$ Hz. We note that, for case 1 (thick dashed lines), the responses tend to their steady-state relatively rapidly after the wavefront has passed. This behaviour is of interest, as the strain imposed on an elastic plate due to a transient periodic excitation can be larger than the frequency-domain analysis suggests. For case 4 (solid lines), the influence of the lateral boundaries becomes apparent through the longer response-time. While it takes ~ 25 s to reach the steady-state for a frequency $f = 0.87$ Hz in case 1 (see Fig. 7(a)–(c)), the response-time is more than 100 s in case 4. The multiple reflections on the wavemaker and the beach explain this behaviour and similar observations are made for $f = 1.4$ Hz (see Fig. 7(d)–(f)), where the response-time is even larger than at lower frequencies. At this frequency the plate generates more scattering, as can be seen in Fig. 6(c), and the waves travel back and forth between the wavemaker and the plate, and the plate and the beach, before settling to a steady-state.

Note that the case 4 responses reach case 1 steady-state for a short time interval, before the reflected waves re-disturb the system. This means that, while performing experimental tests in a wave tank, i.e. case 4, it is possible to capture the steady-state of case 1 during a time window that depends on the frequency of the incident wave, assuming the plate is located far enough from the boundaries of the tank. This is particularly useful for comparing experimental data to frequency-domain models and this approach has been used by Montiel et al. (2011) to compare their experimental and numerical data. In practice, the efficiency of this experimental approach largely depends on the frequency. In particular, at low frequency ($f < 0.5$ Hz), the incident wave travels quickly through the tank, so the time window is very short or nonexistent, but in this case there is little scattering produced by the plate, so very little interest is given to this regime as part of the large body approximation.

We also note that two major disturbances occur in the response of case 4 before the curves settle down. Those events can be identified as the wavefront of the wave generated by the wavemaker, as in case 1, and a wave that has travelled from the plate to the wavemaker and back to the plate after experiencing reflection. This implies that in most cases the effects of the boundaries are overcome after two reflections only. In Fig. 7(e), this is not true and the steady-state is reached gradually at a time significantly different from the one reached after the second disturbance. Although the response to the second major disturbance may give an idea of the steady-state value, other minor disturbances still occur afterwards. This is particularly true for thick plates, as we can see in Fig. 7(c) and (f), in which cases the multiple reflections affect the response

for a long time, which is related to the fact that thicker plates induce more wave scattering.

The lateral boundaries also affect the time at which the maximum scaled strain energy, $V_{\max}$, say, is obtained. Although the first wavefront always induces a maximum, the multiple reflections may cause the time-response to reach a higher peak subsequently (see Fig. 7(c)). In what follows, we only consider the plate of thickness $h = 5\,\text{mm}$. From the transient response, we can extract characteristic properties that may be analysed over a relevant frequency range. We are particularly interested in the maximum strain energy $V_{\max}$ and the time at which this maximum is reached $t_{\max}$. Fig. 8 displays $V_{\max}$ and $t_{\max}$ over the frequency range $f = 0.5$–$1.5\,\text{Hz}$. Case 1 (unbounded domain) is analysed in Fig. 8(a) and (b). The maximum strain energy (solid line) behaves similarly to the frequency-domain response (dashed line), as we can see in Fig. 8(a), and the difference in magnitude seems to increase with the frequency. We note from Fig. 8(b) that $t_{\max}$ increases monotonically over the spectrum as the frequency rises. In this case the maximum is always reached as the incident wavefront starts exciting the plate, as previously seen in Fig. 7.

Similar results for case 4 (laterally bounded fluid domain) are displayed in Fig. 8(c) and (d). We note that at low frequencies, i.e. $f < 0.9\,\text{Hz}$, $V_{\max}$ and $t_{\max}$ are the same as for case 1, so the initial wave front generates the maximum bending in the plate, as we see in Fig. 7(b). For higher frequencies, there is a succession of peaks in Fig. 8(c), emerging from the curve representing case 1. Relating these peaks to the time at which they occur (see Fig. 8(d)), we note that they correspond to maxima reached later than the time the initial wavefront hits the plate, after reflections on the lateral boundaries.

5.4. Multiple plates analysis

In this section, we investigate the response of multiple identical plates. A first arrangement of four plates of thickness $h = 10\,\text{mm}$ is studied in the time-domain for case 4 (bounded fluid domain). The abscissae of the plates' left edges are 4, 6, 10 and 12 m and the frequency of the wave generated is $f = 1\,\text{Hz}$. Fig. 9 shows the evolution of the plates' displacements and fluid-surface elevations for $t = 1, 5, 10, 15, 20, 25\,\text{s}$. A decrease in the amplitude of flexure of the plates from left to right is clearly visible (for 20 and 25 s). This is a result of the attenuation of wave energy produced by scattering (see, e.g., Kohout and Meylan, 2008). As the system {Plates+Fluid} is conservative, the attenuated energy is reflected back towards the wavemaker (although it is distributed amongst waves with different phases). A more detailed analysis on this multiple plate arrangement would be complex to perform, so that we focus our attention for the remainder of this section on a more fundamental study case.

Consider two identical plates, with properties the same as the single plate case, and focus the present analysis on a single thickness, $h = 5\,\text{mm}$, as the influence of this parameter was studied earlier. We denote the spacing between the two plates as s. Additionally, we set $x_l = 6\,\text{m}$ as the location of the left edge of plate 1; it follows that the right edge of plate 2 is located at $x_r = 9 + s$. It is of use for the analysis of two plates to define the relative strain energy of the system as $V_r = V_2/V_1$, where V_1 and V_2 respectively are the

strain energy of plates 1 and 2.

We choose to remove the reflections from the wavemaker and beach (i.e. case 1). This allows us to determine the interactions of the two plates without interference from the fluid domain's lateral boundaries. In Fig. 10(a) and (c) we show the relative strain energy plotted against frequency for two spacings that are $s = L/3 = 0.5\,\mathrm{m}$ and $s = 3L = 4.5\,\mathrm{m}$, respectively. Fig. 10(b) and (d) display the corresponding reflection coefficient spectra. Similarly to Fig. 6, we look at the relative response of the system over an extended spectrum $f = 0.5$–$3\,\mathrm{Hz}$. For the smaller spacing (Fig. 10(a) and (b)), the relative response oscillates over the spectrum, such that when $V_r > 1$ the flexural motion is dominated by plate 2, while when $V_r < 1$, plate 1's flexure dominates. In the latter case, Fig. 10(b) indicates that the cause is a high reflection coefficient.

For the larger spacing (Fig. 10(c)–(d)), the number of resonances discussed in the previous paragraph is significantly increased, but we observe that the same features are present. The resonances are related to the natural frequencies of the system {Plate 1+Plate 2}. When the spacing increases, harmonics of lower frequencies are allowed to resonate and this is what is demonstrated here. Similar to the smaller spacing, minima of relative strain energy occur for large reflection coefficients. It is also interesting to note that all the curves shown in Fig. 10 fit into an envelope that is the same for both spacings. The important features of this envelope are driven by the spectrum of the single plate. In particular, when comparing with the dashed curve from Fig. 6, we note that the envelope coincides with $V_r = 1$ when the response of a single plate is maximal and when the reflection coefficient of a single plate is zero. The envelopes of the reflection coefficient curves in Fig. 10 are also similar and it is true for any spacing. The behaviour of the reflection coefficient is in agreement with the results given by Williams and Squire (2008) for an open lead. It is also interesting to note that for the frequencies at which we have perfect transmission, we also have $V_r = 1$, i.e. equipartition of the energy in the plates. The reciprocal proposition is, however, not true, i.e. $V_r = 1$ does not always correspond to perfect transmission.

The transient response of the system {Plate 1+Plate 2} is studied for case 1 in the following. Let us define the ratio of the maximal strain energy as $\widetilde{V}_{\max} = V^2_{\max}/V^1_{\max}$, where $V^i_{\max}$ is the scaled strain energy in plate i ($i = 1, 2$). We show $\widetilde{V}_{\max}$ for both spacings in Fig. 11(a) and (b). For comparison, we also define $\widetilde{V}^*_{\max}$, to be the ratio of maximum strain energy experienced by the plates separately, in the absence of the other plate. This quantity is plotted in Fig. 11(a) and (b) as small circles. We note that this quantity is not 1 in general, as the amplitude of the wavefront varies with the distance from the wavemaker. The transient wave generated by the wavemaker is composed of superposed components of different frequencies, which therefore travel at different group velocities, resulting in a time evolution of the wavefront amplitude. We can see that $\widetilde{V}_{\max}$ tends to values less than 1 as f decreases. This low frequency behaviour is clearly due to the transient evolution of the wavefront. At low frequencies very little scattering is occurring and the incident wave travels through the fluid domain unperturbed. This is confirmed by the low frequency spectrum of $\widetilde{V}^*_{\max}$, as we can see in Fig. 11(a) and (b).

For high frequencies, as more scattering is involved, we see in Fig. 11(a) that $\widetilde{V}_{\max} < 1$. It is also apparent that a downward bump is present, forming local sharp corners along the curve. It is found that this bump is associated with a regime in which $V^1_{\max}$ is not reached by the initial wavefront but from the multiple reflections that occur between the plates. For the larger spacing (see Fig. 11(b)), we have 5 downward bumps in this frequency range, that can be explained in a similar way.

6. Conclusions

In this paper, we have derived a solution technique for the transient scattering of a group of thin elastic plates in a two-dimensional laterally bounded fluid domain. Results for the transient response of one or more plates can be found, with the effects of the wavemaker and the reflective beach included. A Fourier transform technique is employed to express the governing equations in the frequency-domain. The solution method for the single frequency harmonic problem is based on calculating a transfer matrix associated with a single plate, accounting for the Archimedean draught, in which evanescent and damped modes are accommodated into expansions of the fluid motion. A version of eigenfunction matching at each edge, accommodating the singular behaviour of the fluid velocity at the plate's sharp corner, is used to calculate the transfer matrix associated with it. It then becomes straightforward to deal with multiple plates. After assimilation of the wavemaker and beach conditions, we obtain a solution for the fluid motion everywhere in the fluid domain.

Numerical results are presented to show the influence of the lateral boundaries on the flexural response of a group of plates in the frequency-domain. In particular, we showed how the wavemaker and the beach affect the response for a single plate over a wide bandwidth. It was found that the general trend of the spectra, including wavemaker and beach, was affected by the response of the same plate in an unbounded domain. The lateral boundaries influence the motion by adding extra resonances in the spectrum associated with the natural modes of the system {Plate+Tank}. The response of a system composed of two identical plates in an unbounded domain showed that extra resonances are also added in this case, depending on the spacing between the plates. The partition of energy between the plates was associated with the reflection coefficient frequency spectrum and it was found that, for perfect transmission, equipartition of energy is confirmed.

The transient response of the system was also analysed. We were particularly interested in the influence of the boundaries, and of having multiple plates, on the maximum bending of the system. It was found that for a single plate, the transient response is characterised by a maximum that is always reached, as the initial wavefront excites the plate. The lateral boundaries of the fluid domain induce multiple reflections, so the plate experiences further transient disturbances that may cause a maximum bending of larger magnitude than the one due to the initial wavefront. In the study of ocean waves interactions with frozen ocean, the results obtained suggest ice floes may experience large strains due to a transient excitation and knowing the

response in the frequency-domain may not be sufficient to forecast the likelihood of fracture.

The authors are aware that real wave tank experiments would generate three-dimensional effects that are not present in this model. Indeed, to reproduce accurately all the phenomena involved in wave tank experiments, the present model would need to be extended to a three-dimensional one that includes the effect of the lateral boundaries. Studies are on the way to reproduce numerically transient hydroelastic tests performed in real wave tanks under linear wave conditions. The mapping from the time to frequency-domain introduced in §3 is still valid in that case, and a solution method for the harmonic three-dimensional problem is only required. In the meantime, we can remove the influence of the lateral boundaries in experimental tests by defining a time window in which the steady-state is captured before the reflected waves contaminate the response. This approach has proved to be very efficient (see Montiel et al., 2011) when the wavelength is comparable to or smaller than the plate's diameter, i.e. the large body assumption holds.

Acknowledgments

FM was supported by a University of Otago Doctoral Scholarship. The authors gratefully acknowledge the support of the Marsden Fund Council from Government funding administered by the Royal Society of New Zealand. They also greatly appreciated useful discussions on the topic of wave generation in a wave tank with Félicien Bonnefoy and are in debt to the reviewers for their suggestions.

A. Expansion of the free edge conditions

Using Eq. (13e), we can expand the 4 free edge conditions applied to $\widehat{\Phi} = \widehat{\Phi}^{(+)} + \widehat{\Phi}^{(-)}$, as

$$\sum_{n=-2}^{N} \kappa_n^3 \left\{ \left[A^{(+)}\right]_n + \left[A^{(-)}\right]_n \mathrm{e}^{-\kappa_n\left(x_2^{(-)}-x_2^{(+)}\right)} \right\} \tan\kappa_n\,(H-d) = 0 \tag{34a}$$

$$\sum_{n=-2}^{N} \kappa_n^3 \left\{ \left[A^{(+)}\right]_n \mathrm{e}^{-\kappa_n\left(x_2^{(-)}-x_2^{(+)}\right)} + \left[A^{(-)}\right]_n \right\} \tan\kappa_n\,(H-d) = 0 \tag{34b}$$

$$\sum_{n=-2}^{N} \kappa_n^4 \left\{ \left[A^{(+)}\right]_n - \left[A^{(-)}\right]_n \mathrm{e}^{-\kappa_n\left(x_2^{(-)}-x_2^{(+)}\right)} \right\} \tan\kappa_n\,(H-d) = 0 \tag{34c}$$

$$\sum_{n=-2}^{N} \kappa_n^4 \left\{ -\left[A^{(+)}\right]_n \mathrm{e}^{-\kappa_n\left(x_2^{(-)}-x_2^{(+)}\right)} + \left[A^{(-)}\right]_n \right\} \tan\kappa_n\,(H-d) = 0 \tag{34d}$$

These conditions allow us to express the amplitudes of damped modes, $\left[A^{(\pm)}\right]_{-j}$ $(j = 1, 2)$, in terms of $\left[A^{(\pm)}\right]_n$, $n = 0, \ldots, N$. We first define the following sequences

$$L_n^{(1)} = \kappa_n^3 \tan\kappa_n\,(H-d)\,, \quad L_n^{(2)} = \kappa_n^3\, \mathrm{e}^{-\kappa_n\left(x_2^{(-)}-x_2^{(+)}\right)} \tan\kappa_n\,(H-d)\,,$$

$$L_n^{(3)} = \kappa_n^4 \tan\kappa_n\,(H-d)\,, \quad L_n^{(4)} = -\kappa_n^4\, \mathrm{e}^{-\kappa_n\left(x_2^{(-)}-x_2^{(+)}\right)} \tan\kappa_n\,(H-d)\,,$$

for $n = -2, \ldots, N$.

The amplitudes of the damped modes are then taken out of the sums in Eqs. (34). Combining Eqs. (34a) and (34b) into a single matrix equation gives

$$\begin{pmatrix} L_{-2}^{(1)} & L_{-1}^{(1)} \\ L_{-2}^{(2)} & L_{-1}^{(2)} \end{pmatrix} \mathbf{A}^{*(+)} + \begin{pmatrix} L_{-2}^{(2)} & L_{-1}^{(2)} \\ L_{-2}^{(1)} & L_{-1}^{(1)} \end{pmatrix} \mathbf{A}^{*(-)} + \begin{pmatrix} L_{0}^{(1)} & \ldots & L_{N}^{(1)} \\ L_{0}^{(2)} & \ldots & L_{N}^{(2)} \end{pmatrix} \mathbf{A}^{(+)} + \begin{pmatrix} L_{0}^{(2)} & \ldots & L_{N}^{(2)} \\ L_{0}^{(1)} & \ldots & L_{N}^{(1)} \end{pmatrix} \mathbf{A}^{(-)} = 0, \tag{35}$$

where

$$\mathbf{A}^{*(\pm)} = \left(\left[A^{(\pm)} \right]_{-2}, \left[A^{(\pm)} \right]_{-1} \right)^{\mathrm{T}}.$$

Likewise, combining Eqs. (34c) and (34d) gives

$$\begin{pmatrix} L_{-2}^{(3)} & L_{-1}^{(3)} \\ L_{-2}^{(4)} & L_{-1}^{(4)} \end{pmatrix} \mathbf{A}^{*(+)} + \begin{pmatrix} L_{-2}^{(4)} & L_{-1}^{(4)} \\ L_{-2}^{(3)} & L_{-1}^{(3)} \end{pmatrix} \mathbf{A}^{*(-)} + \begin{pmatrix} L_{0}^{(3)} & \ldots & L_{N}^{(3)} \\ L_{0}^{(4)} & \ldots & L_{N}^{(4)} \end{pmatrix} \mathbf{A}^{(+)} + \begin{pmatrix} L_{0}^{(4)} & \ldots & L_{N}^{(4)} \\ L_{0}^{(3)} & \ldots & L_{N}^{(3)} \end{pmatrix} \mathbf{A}^{(-)} = 0, \tag{36}$$

We solve the system defined by Eqs. (35) and (36) for the 2-length vectors $\mathbf{A}^{*(\pm)}$ straightforwardly, assuming that the square matrices weighting the vectors $\mathbf{A}^{*(\pm)}$ are invertible, which gives

$$\mathbf{A}^{*(\pm)} = \mathbf{T}_1^{\pm} \mathbf{A}^{(+)} + \mathbf{T}_2^{\pm} \mathbf{A}^{(-)},$$

where

$$\mathbf{T}_i^{\pm} = \begin{pmatrix} \mathbf{T}_{i2}^{\pm} \\ \\ \mathbf{T}_{i1}^{\pm} \end{pmatrix}, \quad i = 1, 2.$$

References

Abramowitz, M., Stegun, I. A., 1970. Handbook of Mathematical Functions. Dover.

Bennetts, L. G., 2007. Wave scattering by ice sheets of varying thickness. Ph.D. thesis, University of Reading.

Bennetts, L. G., Biggs, N. R. T., Porter, D., 2007. A multi-mode approximation to wave scattering by ice sheets of varying thickness. Journal of Fluid Mechanics. 579,413-443.

Bennetts, L. G., Biggs, N. R. T., Porter, D., 2009. The interaction of flexural-gravity waves with periodic geometries. Wave Motion. 46, 57-73.

Bennetts, L. G., Squire, V. A., 2009. Wave scattering by multiple rows of circular ice floes. Journal of Fluid Mechanics. 639, 213–238.

Bennetts, L. G., Peter, M. A., Squire, V. A., Meylan, M. H., 2010. A three-dimensional model of wave attenuation in the marginal ice zone. Journal of Geophysical Research. Oceans 115, C12043.

Bennetts, L. G., Williams, T. D., 2010. Wave scattering by ice floes and polynyas of arbitrary shape. Journal of Fluid Mechanics. 662, 5–35.

Bonnefoy, F., Le Touzé, D., Ferrant, P., 2006. A fully-spectral 3D time-domain model for second-order simulation of wavetank experiments. Part B: Validation, calibration versus experiments and sample applications. Applied Ocean Research. 28, 121–132.

Chung, H., Fox, C., 2002. Calculation of wave-ice interaction using the Wiener-Hopf technique. New Zealand Journal of Mathematics. 31, 1–18.

Clément, A., 1996. Coupling of two absorbing boundary conditions for 2D time-domain simulations of free surface gravity waves. Journal of Computational Physics. 126, 139–151.

Fox, C., Squire, V. A., 1994. On the oblique reflexion and transmission of ocean waves at shore fast sea ice. Philosophical Transactions of The Royal Society A- Mathematical Physical and Engineering Sciences. 347, 185–218.

Hazard, C., Meylan, M. H., 2007. Spectral theory for an elastic thin plate floating on water of finite depth. SIAM Journal on Applied Mathematics. 68, 629–647.

Kagemoto, M., Fujino, M., Murai, M., 1998. Theoretical and experimental predictions of the hydroelastic response of a very large floating structure in waves. Applied Ocean Research. 20, 135–144.

Kashiwagi, M., 2000a. Research on hydroelastic response of VLFS: recent progress and future work. International Journal of Offshore and Polar Engineering. 10, 81–90.

Kashiwagi, M., 2000b. A time-domain mode-expansion method for calculating transient elastic responses of a pontoon-type VLFS. Journal of Marine Science and Technology. 5, 89–100.

Kohout, A., Meylan, M. H., Sakai, S., Hanai, K., Leman, P., Brossard, D., 2007. Linear water wave propagation through multiple floating elastic plates of variable properties. Journal of Fluids and Structures. 23, 649–663.

Kohout, A., Meylan, M. H., 2008. An elastic plate model for wave attenuation and ice floe breaking in the marginal ice zone. Journal of Geophysical Research. Oceans 113, C09016.

Korobkin, A., 2000. Unsteady hydroelasticity of floating plates. Journal of Fluids and Structures. 14, 971–991.

Linton, C. M., Chung, H., 2003. Reflection and transmission at ocean/sea-ice boundary. Wave Motion. 38 43–52.

Linton, C. M., McIver, P., 2001. Handbook of mathematical techniques for wave/structure interactions. Chapman & Hall /CRC, Boca Raton, Florida.

Meylan, M. H., 2002. Wave response of an ice floe of arbitrary geometry. Journal of Geophysical Research. Oceans 107, 3005.

Meylan, M. H., Squire, V. A., 1994. The response of ice floes to ocean waves. Journal of Geophysical Research. Oceans 99, 891–900.

Meylan, M. H., Sturova, I. V., 2009. Time-dependent motion of a two-dimensional floating elastic plate. Journal of Fluids and Structures. 25, 445–460.

Montiel, F., Bonnefoy, F., Bennetts, L. G., Squire, V. A., Ferrant, P., Marsault, P., 2011. Experimental validation of a linear numerical model for the water wave scattering by a compliant floating elastic disk. In: Proceedings of the 26th International Workshop on Water Waves and Floating Bodies, Athens, Greece, 117–120.

Ohta, M., Ikegami, K., Yamaguchi, Y., 1997. Experimental study on elastic behaviour of a huge floating structure in waves (in Japanese). Transactions of West-Japan Society of Naval Architects. 95, 99–108.

Ooura, T., 2005. A double exponential formula for the Fourier transforms. Publications of the Research Institute for Mathematical Sciences. 41, 971–977.

Peter, M. A., Meylan, M. H., Chung, H., 2003. Wave scattering by a circular plate in water of finite depth: a closed form solution. In: Proceedings of the thirteenth international offshore and polar engineering conference, 180–185.

Peter, M. A., Meylan, M. H., 2004. Infinite-depth interaction theory for arbitrary floating bodies applied to wave forcing of ice floes. Journal of Fluid Mechanics. 500, 145–167.

Roux de Reilhac, P., Bonnefoy, F., Rousset, J. M., Ferrant, P., 2011. Improved transient water wave technique for the experimental estimation of ship responses. Journal of Fluids and Structures. 27, 456–466.

Sakai, S., Hanai, K., 2002. Empirical formula of dispersion relation of waves in sea ice. In: Ice in the environment. Proceedings of the 16th IAHR International Symposium on Ice. 327–335.

Schäffer, H. A., 1996. Second-order wavemaker theory for irregular waves. Ocean Engineering. 23, 47–88.

Squire, V. A., 2007. Of ocean waves and sea-ice revisited. Cold Regions Science and Technology. 49, 110–133.

Squire, V. A., Dugan, J. P., Wadhams, P., Rottier, P. J., Liu, A. K., 1995. Of ocean waves and sea ice. Annual Review of Fluid Mechanics. 27, 115–168.

Sturova, I. V., 2006. Unsteady behavior of an elastic beam floating on the surface of an infinitely deep fluid. Journal of Applied Mechanics and Technical Physics. 47, 71–78.

Timoshenko, S., Woinowsky-Krieger, S., 1959. Theory of plates and shells. McGraw-Hill.

Watanabe, E., Utsunomiya, T., Wang, C. M., 2004. Hydroelastic analysis of pontoon-type VLFS: a literature survey. Engineering Structures. 26, 245–256.

Williams, T. D., Porter, R., 2009. The effect of submergence on the scattering by the interface between two semi-infinite sheets. Journal of Fluids and Structures. 25, 777–793.

Williams, T. D., Squire, V. A., 2008. The effect of submergence on wave scattering across a transition between two floating flexible plates. Wave Motion. 45, 361–379.

Yago, K. and Endo, H., 1996. On the hydroelastic response of box-shaped floating structure with shallow draft (in Japanese). Journal of the Society of Naval Architects of Japan. 180, 341–352.

Figures

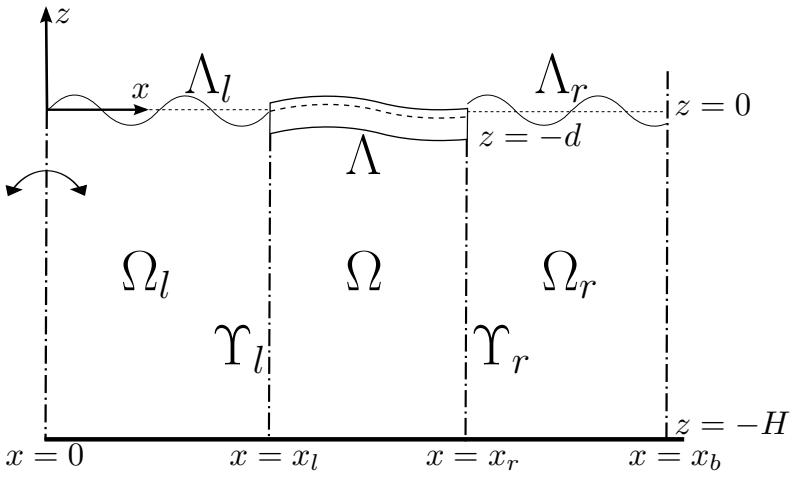

Figure 1: Schematic diagram of the geometry.

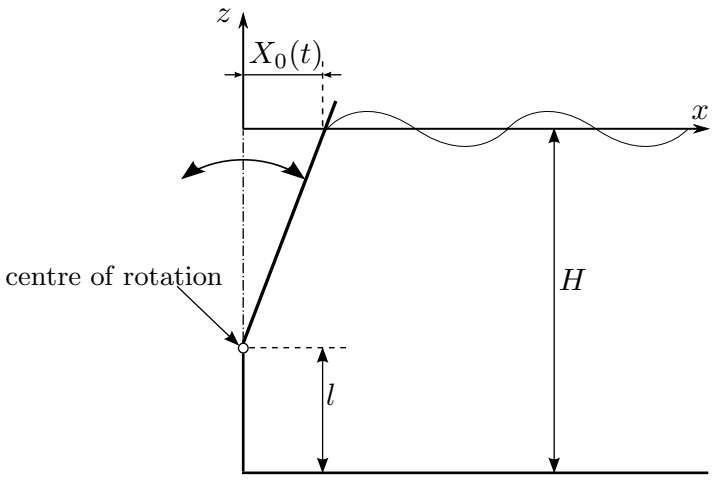

Figure 2: Schematic diagram of a typical hinged-flap wavemaker. Its motion is linearised about the z-axis and is characterised by the position of the centre of rotation, located at $z = l - H$, and its amplitude at $z = 0$, $X_0(t)$.

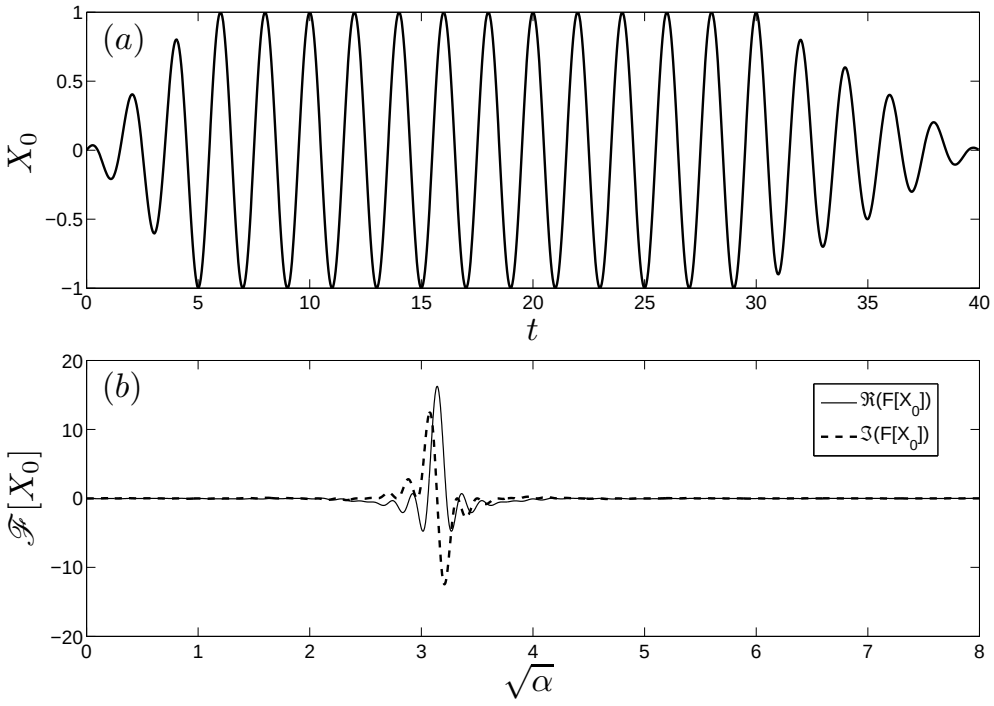

Figure 3: Wavemaker amplitude (a) time evolution profile and (b) spectral distribution (Fourier transform).

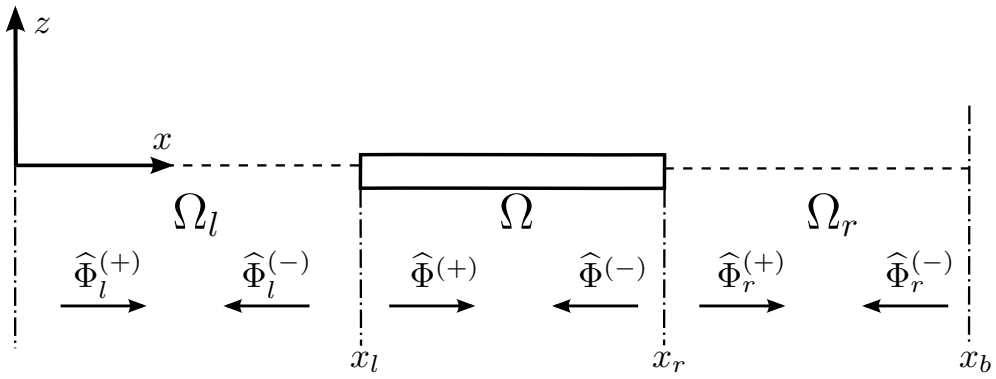

Figure 4: Decomposition of the potential in the three subdomains of the fluid domain. The arrows indicate the directions of propagation of the corresponding potential.

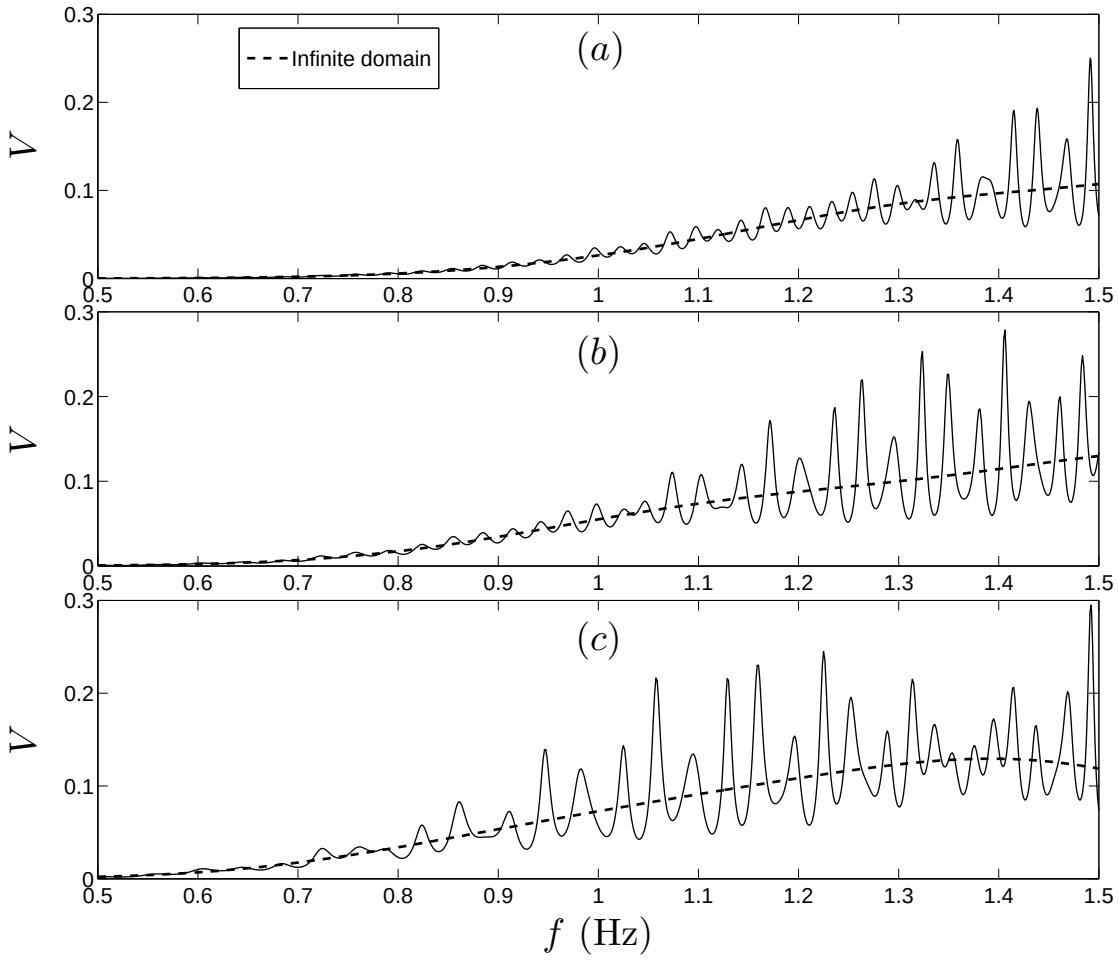

Figure 5: Strain energy of a single plate as a function of frequency. Results are given for an infinite domain (thick dashed curves) and for a bounded fluid domain (solid). The spectra are given for (a) $h = 3\,\mathrm{mm}$, (b) $h = 5\,\mathrm{mm}$ and (c) $h = 10\,\mathrm{mm}$.

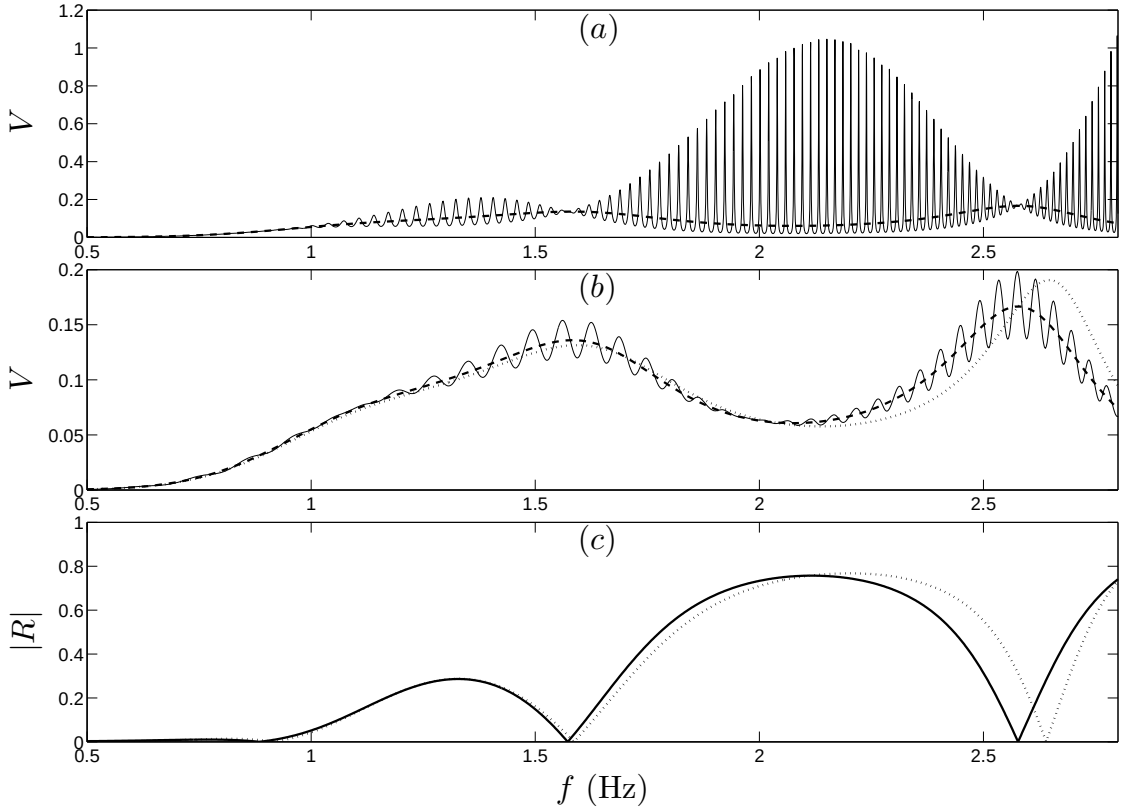

Figure 6: Same as Fig. 5(b) for (a) case 2 (solid line) and (b) case 3 (solid line). In both figures, case 1 is given for reference (thick dashed line). The reflection coefficient spectrum of the plate in an unbounded domain is given in (c). The strain energy and reflection coefficient spectra in the case of the shallow-draught approximation (dotted lines) are given in (b) and (c), respectively.

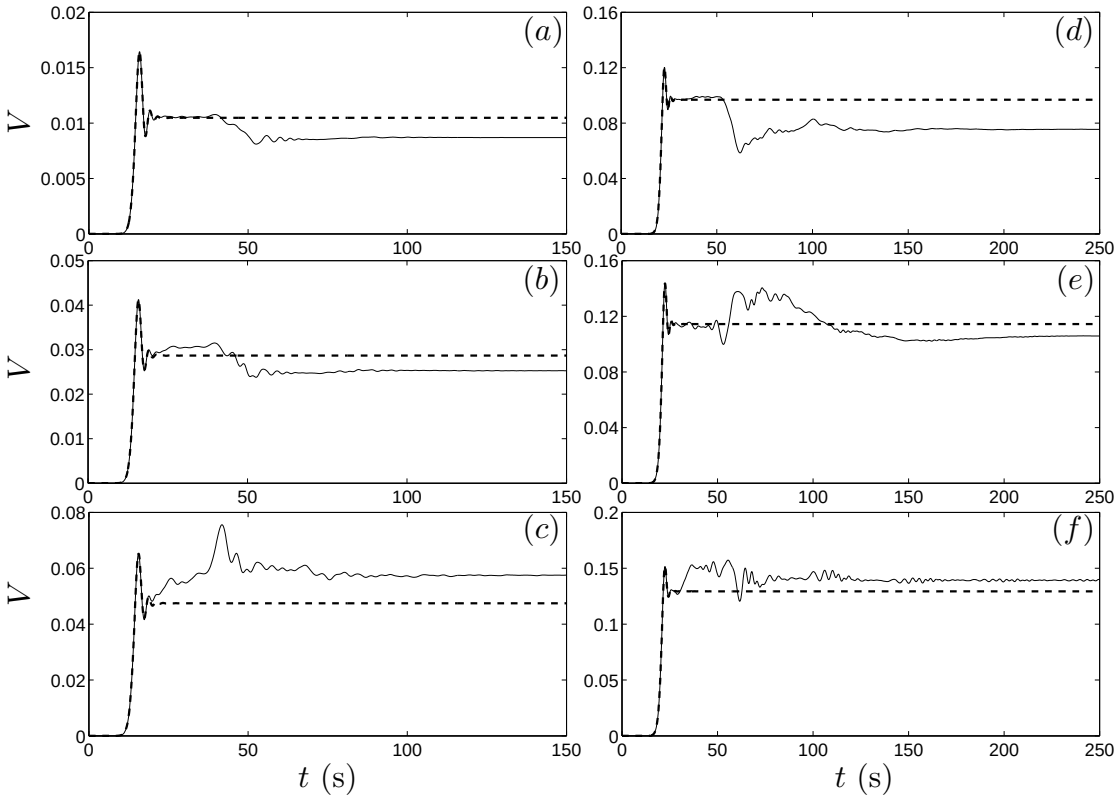

Figure 7: Scaled strain energy versus time in a plate of thickness $h = 3\,\text{mm}$ ((a) and (d)), $h = 5\,\text{mm}$ ((b) and (e)) and $h = 10\,\text{mm}$ ((c) and (f)). Case 1 (unbounded domain) is represented by a thick dashed line and case 4 (bounded fluid domain) is represented by a solid line. The responses are given for frequencies $f = 0.87\,\text{Hz}$ ((a)–(c)) and $f = 1.4\,\text{Hz}$ ((d)–(f)).

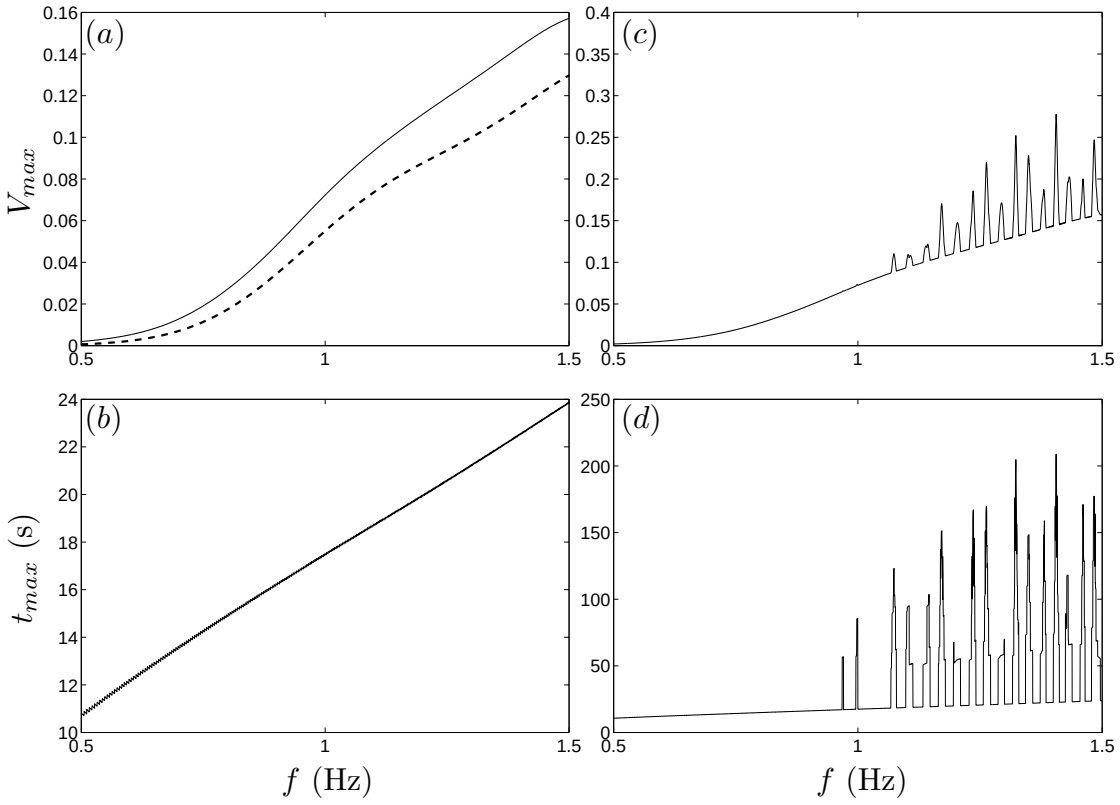

Figure 8: Time/frequency analysis for a single plate of thickness $h = 5\,\text{mm}$, in cases 1 ((a) and (b)) and 4 ((c) and (d)). The properties herein analysed are ((a) and (c)) the maximum strain energy (solid line), with the frequency response (dashed line) given for comparison in (a) and ((b) and (d)) the time at which this maximum is reached (solid line).

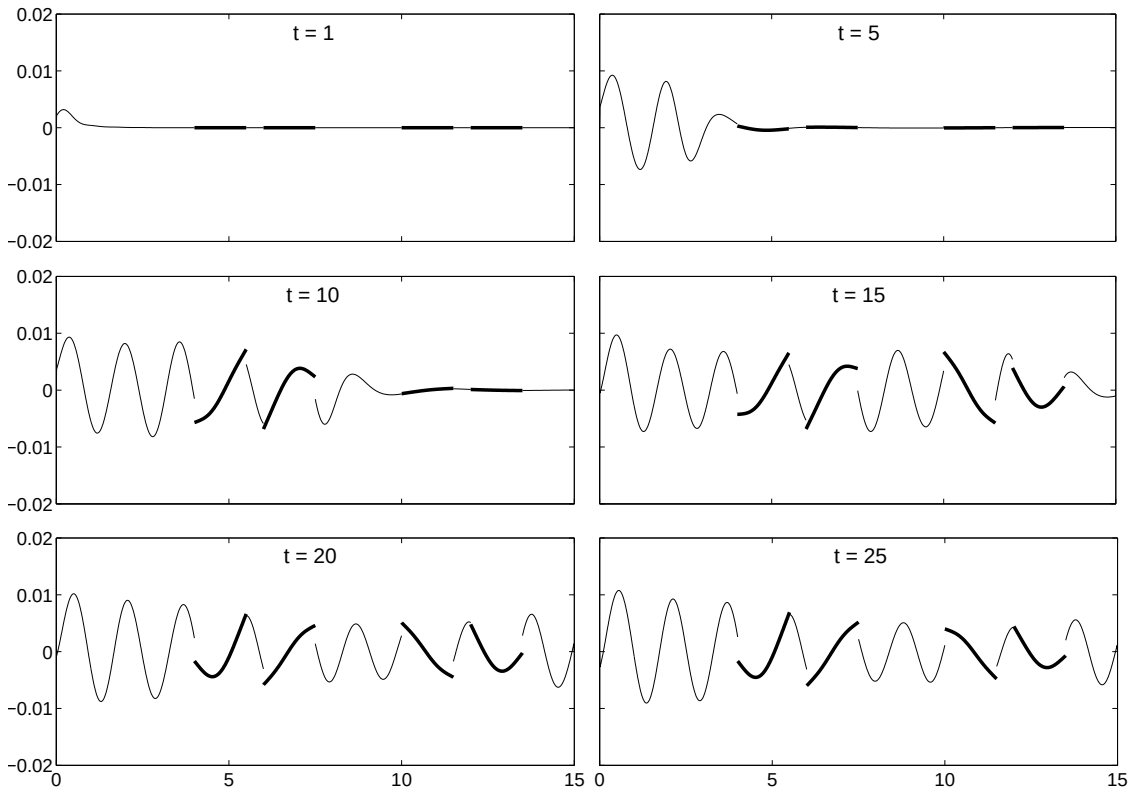

Figure 9: Snapshots of the transient response of an arrangement of 4 identical plates. The frequency of the generated waves is $f = 1\,\mathrm{Hz}$ and the steady-state wave steepness is $\epsilon = 1\%$.

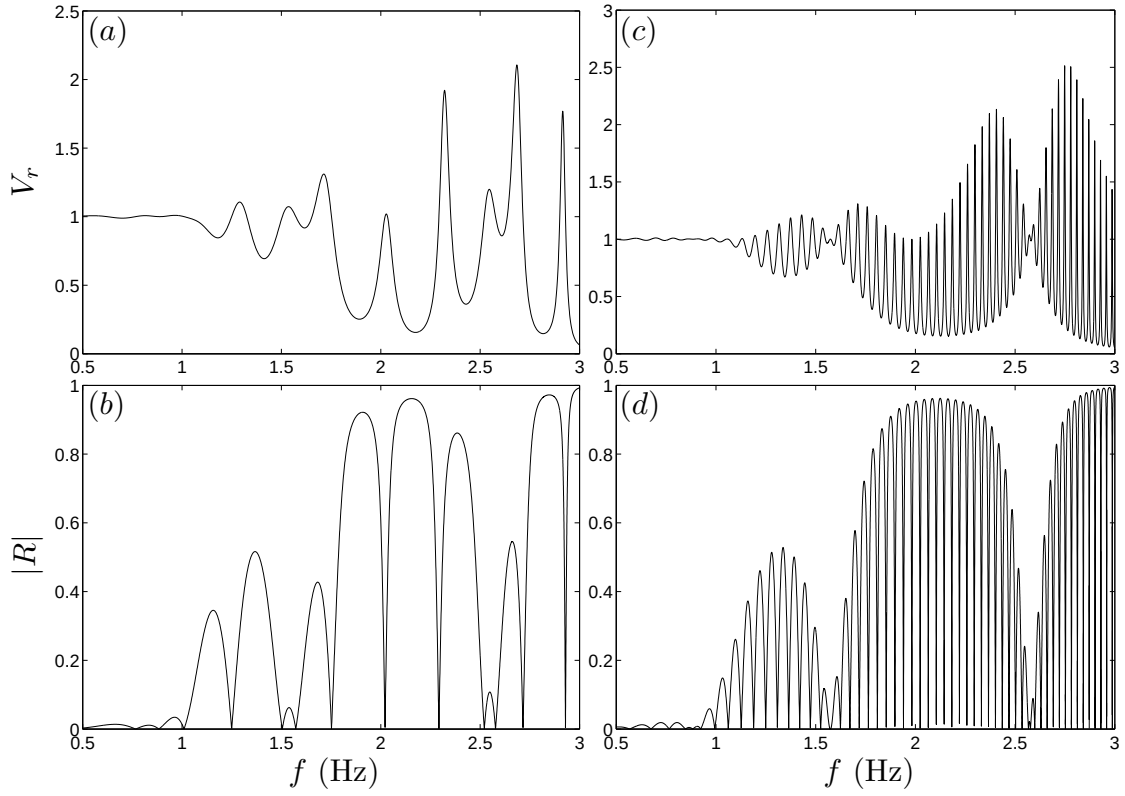

Figure 10: Relative strain energy ((a) and (c)) and reflection coefficient ((b) and (d)) of the two-plates system as a function of frequency for case 1. The spacing between the two plates is ((a) and (b)) $s = 0.5\,\mathrm{m}$ and ((c) and (d)) $s = 4.5\,\mathrm{m}$.

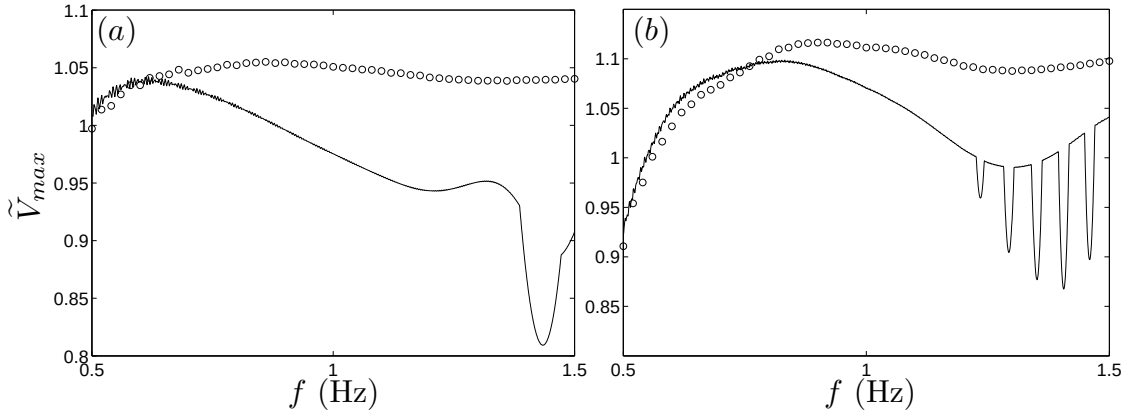

Figure 11: Ratio of maximum strain energy (solid line) for two identical plates of thickness $h = 5\,\mathrm{mm}$, for the spacings (a) $s = 0.5\,\mathrm{m}$ and (b) $s = 4.5\,\mathrm{m}$ in the frequency range $f = 0.5$–$1.5\,\mathrm{Hz}$. The ratio of maximum strain energy of the individual single plate problems are also plotted as circles.